Accepted Manuscript

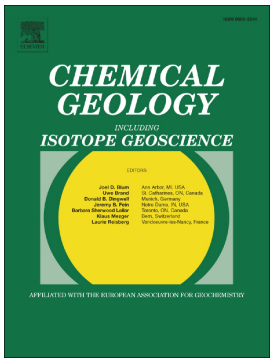

Linking the bitter springs carbon isotope anomaly and early neoproterozoic oxygenation through I/[Ca+Mg] ratios

Sarah Wörndle, Peter W. Crockford, Marcus Kunzmann, Thi Hao Bui, Galen P. Halverson

PII: S0009-2541(19)30310-9
DOI: https://doi.org/10.1016/j.chemgeo.2019.06.015
Reference: CHEMGE 19215

To appear in: *Chemical Geology*

Received date: 9 June 2018
Revised date: 2 June 2019
Accepted date: 12 June 2019

Please cite this article as: S. Wörndle, P.W. Crockford, M. Kunzmann, et al., Linking the bitter springs carbon isotope anomaly and early neoproterozoic oxygenation through I/[Ca+Mg] ratios, Chemical Geology, https://doi.org/10.1016/j.chemgeo.2019.06.015

Linking the Bitter Springs Carbon Isotope Anomaly and early Neoproterozoic Oxygenation through I/[Ca+Mg] ratios

Sarah Wörndle[a,*], Peter W. Crockford[b,c], Marcus Kunzmann[d], Thi Hao Bui[a], Galen P. Halverson[a,e]

[a] Department of Earth and Planetary Sciences, McGill University, 3450 University St., Montreal QC H3A 0E8, Canada
[b] Department of Earth and Planetary Sciences, Weizmann Institute of Science, Rehovot 76100 Israel
[c] Department of Geosciences, Guyot Hall, Princeton, NJ 08544, United States
[d] CSIRO Mineral Resources, Australian Resources Research Centre, Kensington, WA 6151, Australia
[e] Earth Dynamics Research Group, The Institute for Geoscience Research (TIGeR), School of Earth and Planetary Sciences, Curtin University, GPO Box U1987, Perth, WA 6845, Australia

[*]Corresponding author.
E-mail address: sarah.worndle@mail.mcgill.ca (Sarah Wörndle)

Keywords: Stable isotope geochemistry, Carbonates, Tonian, East-Greenland, East-Svalbard, Mackenzie Mountains, I/[Ca+Mg].

ABSTRACT

The ca. 810 Ma Bitter Springs carbon isotope anomaly is an abrupt and long-lived (5–10 Myr.) departure from the positive carbon isotope values ($\delta^{13}C_{carb}$) that otherwise characterize early-middle Neoproterozoic carbonate rocks. The onset of this isotope anomaly is manifested by a globally expressed ~8‰ negative shift in $\delta^{13}C$ values in shallow marine carbonate strata. Given increasing evidence that metazoan diversification began well before the Ediacaran Period, the Bitter Springs anomaly is a logical interval to explore the potential relationship between biological innovation, perturbations to the carbon cycle, and oxygenation. The iodine-to-calcium+magnesium ratio (I/[Ca+Mg]) in marine carbonates is a sensitive proxy for seawater redox conditions that is increasingly being applied to reconstruct the oxygenation of the global surface ocean through Earth's history. We report I/[Ca+Mg] ratios, along with

carbon and oxygen isotope ratios and major and minor element concentrations from carbonate sections spanning the Bitter Springs anomaly in Svalbard, East Greenland, and the Mackenzie Mountains (northwestern Canada). The results from Svalbard and Greenland collectively show two prominent features. The early stage of the Bitter Springs anomaly is characterized by a negative $\delta^{13}C$ shift coupled to low I/[Ca+Mg] ratios compared to carbonates pre- and post-dating the Bitter Springs anomaly. The last stage of the Bitter Springs anomaly displays a positive excursion in I/[Ca+Mg], with the highest values at ~7 μmol/mol yet documented in rocks older than 580 Ma. In contrast, carbonates from the Mackenzie Mountains are uniformly low and display no variation in I/[Ca+Mg] across the Bitter Springs anomaly, which we interpret to be the consequence of alteration of primary signatures during diagenesis. The observed geochemical variations in our Svalbard and Greenland datasets are interpreted to be the result of a shift from pre-Bitter Springs ocean conditions, defined by well oxygenated surface waters and anoxic-ferruginous bottom waters, to syn-Bitter Springs ocean conditions, characterized by expanded euxinia.

1. Introduction

Atmospheric and oceanic oxygen inventories increased in the Proterozoic from Archean levels, and by the end of the eon, eukaryotes had diversified and given rise to complex predatory Metazoans in an increasingly productive biosphere (Brocks et al., 2017; Butterfield, 2009; Knoll, 1992a; Knoll and Sperling, 2014; Knoll and Walker, 1990; Planavsky et al., 2014; Crockford et al., 2019). Consequently, it is commonly assumed that oxygen levels rose during the Neoproterozoic Era (1000–541 Ma) in what is often referred to as the Neoproterozoic Oxygenation Event (NOE; Canfield et al., 2007; Och and Shields-Zhou, 2012; Planavsky et al., 2014). Although the general pattern of oxygenation across the Proterozoic is broadly agreed upon (Cole et al., 2016; Des Marais et al., 1992; Holland, 2006; Knoll, 2003; Kunzmann et al., 2017a; Kunzmann et al., 2017b; Kunzmann et al., 2015; Lyons et al., 2014; Planavsky et al., 2014; Stolper and Keller, 2018), both the mechanism and timing of the NOE remain controversial. This enduring enigma of Neoproterozoic oxygenation is sustained by the absence of direct proxies for both atmospheric and dissolved oxygen inventories. An emerging consensus is that only through combining diverse redox proxies applied globally (Sperling et al., 2015) will we be able to test and reconcile existing models for Neoproterozoic oxygenation.

The Neoproterozoic, in particular the interval from ca. 850 Ma to 640 Ma, is well known for its high average carbon isotope values in marine carbonates ($\delta^{13}C_{carb}$) (Halverson et al., 2005; Kaufman et al., 1997). In the classic interpretation of ancient carbon isotopes in marine carbonates, it is assumed that highly positive $\delta^{13}C_{carb}$ values reflect high $\delta^{13}C$ values of the seawater dissolved inorganic carbon (DIC) reservoir and that such values are a consequence of a sustained high fractional burial of organic carbon (f_{org}; Kump, 1991; Kump and Arthur, 1999). This organic carbon burial, in turn, is stoichiometrically balanced mole-for-mole by the release and accumulation of O_2 or equivalent oxidizing capacity in the atmosphere and oceans (Des Marais et al., 1992). Following this logic, the first half of the Neoproterozoic (i.e., the Tonian period = 1000–717 Ma) should have experienced a long-term increase in free O_2 or its oxidative equivalent in sulfate and ferric oxides (Crockford et al., 2019). However, in the absence of unambiguous evidence for this increase in oxygen, multiple alternative interpretations have been proposed to account for the high $\delta^{13}C_{carb}$ values in the Tonian period. For example, they may record deposition of ^{13}C-depleted authigenic carbonate

rather than organic carbon (Schrag et al., 2013). Alternatively, Shields and Mills (2017) argued that positive $\delta^{13}C$ excursions in the Neoproterozoic were the natural consequence of a rise in carbonate weathering rather than an increase of f_{org}. Another possibility is that shallow marine carbonate records, while expressing similar isotopic characteristics between one another, are disconnected from the global marine DIC pool, and thus only record processes common to shallow marine carbonate platforms (Immenhauser et al., 2003; Swart, 2008; Higgins et al., 2018). In light of these challenges to the paradigm linking organic carbon burial to the marine $\delta^{13}C_{carb}$ record, it is necessary to test the Neoproterozoic record of large fluctuations in carbon isotopes with evidence for changing f_{org} and O_2 abundance.

The Bitter Springs carbon isotope anomaly (BSA) is an abrupt and long-lived departure from the high $\delta^{13}C_{carb}$ values that otherwise characterize the Tonian period (Halverson et al., 2005; Swanson-Hysell et al., 2015). Although the BSA is named after the Bitter Springs Formation in central Australia where it was first documented (Hill and Walter, 2000), it was later correlated with other basins, one of which is the superbly preserved ca. 820–750 Ma Akademikerbreen Group in northeastern Svalbard (e.g., Halverson et al., 2005, 2007, 2018). In Svalbard, the BSA is defined by an ~8‰ negative shift at ca. 810 Ma followed by an ~8 Myr interval of dominantly low (< 0‰) average $\delta^{13}C_{carb}$ values, and then a shift at ca. 802 Ma back to the highly positive $\delta^{13}C_{carb}$ values that are typical of Tonian carbonates. Given increasing evidence for accelerated eukaryotic diversification during the middle Tonian (Knoll, 2014; Cohen and Macdonald, 2015; Riedman and Saddler, 2017) and a possible rise in atmospheric O_2 and primary productivity around the same time (Cole et al., 2016; Planavsky et al., 2014; Crockford et al., 2019), the BSA is a logical interval to probe early Neoproterozoic redox changes and links to the $\delta^{13}C_{carb}$ record.

A promising new proxy for interrogating ancient marine redox conditions is the ratio of iodine-to-calcium-magnesium (I/[Ca+Mg]) (Hardisty et al., 2014, 2017). Iodine (I) can exist in several oxidation states. The most thermodynamically stable inorganic forms of iodine in seawater are iodate (IO_3^-) and iodide (I^-; Tsunogai and Sase, 1969). Low dissolved iodate concentrations measured in carbonate sediments have been proposed to record low dissolved oxygen concentrations of surface waters in modern and ancient carbonates (Lu et al., 2010, 2017, 2018; Hardisty et al., 2014, 2017). Because the standard redox potential of the couple IO_3^-/I^- (Eh = +1.08V) is very similar to O_2/H_2O (Eh = +1.23V), it is one of the most sensitive elements to changes in

redox conditions in the ocean after manganese (Eh = +1.22V) but before nitrogen (Eh = +0.84V) redox couples (Lu et al., 2010). Along with acting as a highly redox-sensitive element, iodate (the oxidized form of iodine) is easily incorporated into the structure of calcium carbonate minerals where it can substitute for the carbonate ion (Feng and Redfern, 2018; Kerisit et al., 2018; Podder et al., 2017). Hence, the I/Ca ratio measured in calcite has been demonstrated experimentally to have a positive relationship with iodate concentration in the ocean and thus to reflect the concentration of iodate in seawater during calcite precipitation (Lu et al., 2010). Specifically, the I/Ca ratio measured in modern planktonic foraminifera with values of ~5 μmol/mol indicates well oxygenated water, whereas the I/Ca ratio in O_2-depleted waters of an oxygen minimum zone (OMZ) is considerably lower with a ratio between 0.5 and 2.5 μmol/mol (Glock et al., 2014; Lu et al., 2016).

This ratio was applied for the first time as a paleo-redox proxy for shallow marine carbonates deposited during Cretaceous Oceanic Anoxic Events (OAEs; Lu et al., 2010). The I/[Ca+Mg] proxy was also applied on shallow carbonates from the middle Archean to late Proterozoic spanning major events such as the ca. 2.4 Ga Great Oxidation Event (GOE), the ca. 2.3–2.2 Ga Lomagundi positive carbon isotope excursion, and the ca. 570 Ma Shuram negative carbon isotope excursion (Hardisty et al., 2014, 2017). These results suggest that the I/[Ca+Mg] ratio in carbonates may reflect fluctuations in local seawater redox conditions with possible global implications and that this signal can be preserved for billions of years in carbonate rocks. The I/[Ca+Mg] proxy was previously applied to the BSA, and it was concluded that data from Svalbard were consistent with increased but possibly transient surface ocean oxygenation ca. 810 Ma (Lu et al., 2017, 2018). Here we build upon this prior study with additional data from Svalbard, East Greenland, and the Mackenzie Mountains of northwestern Canada. As these formations have witnessed different degrees of diagenetic alteration, this combined data set allows us to explore the effects of post-depositional processes on I/[Ca+Mg] and better ascertain the robustness of the I/[Ca+Mg] proxy in its application to understanding Neoproterozoic oxygenation.

2. Geological setting

2.1. Northeastern Svalbard and East Greenland

Northeastern Svalbard contains a well-preserved Neoproterozoic succession that outcrops in a north-south trending fold and thrust belt spanning from Olav V Land on Spitsbergen to western Nordaustlandet (Fig. 1). The poorly studied Veteranen Group, which comprises dominantly marginal marine siliciclastic rocks along with minor carbonate, forms the base of the Neoproterozoic succession. It is conformably overlain by the ca. 820–750 Ma Akademikerbreen Group, which consists of nearly 2 km of carbonate with minor fine siliciclastic sediments deposited in a stable, thermally subsiding basin (Halverson et al., 2018; Maloof et al., 2006). The Akademikerbreen Group is succeeded conformably by the mixed siliciclastic-carbonate Polarisbreen Group, which includes a record of both the Sturtian and Marinoan glaciations but lacks a record of the middle Ediacaran (Gaskiers) glaciation or Ediacaran biota due to a major erosional unconformity below overlying Paleozoic strata (Knoll and Swett, 1987; Halverson et al., 2004). A strikingly similar stratigraphic succession, albeit thicker and with a greater abundance of siliciclastic strata, occurs in the East Greenland Caledonides (i.e., the Eleonore Bay and Tillite groups; Caby and Bertrand-Safarti, 1988; Hambrey and Spencer, 1987; Katz, 1961; Tirsgaard and Sønderholm, 1997). Given the close stratigraphic similarities between these two regions, both Neoproterozoic successions are widely believed to represent a single, large, stable platform (informally referred to as the East Greenland-East Svalbard or EGES basin) on the northeastern margin of Greenland (Fairchild and Hambrey, 1995; Halverson et al., 2005; Hoffman et al., 2012).

The Akademikerbreen Group comprises four formations (from bottom to top: Grusdievbreen, Svanbergfjellet, Draken, Backlundtoppen; Fig. 1) deposited on a broad, tropical, carbonate platform (Maloof et al., 2006). The thick (ca. 600 m) Grusdievbreen Formation is informally subdivided into a lower and upper member. Both are predominantly composed of limestone, with minor dolostone, siltstone and mudstone, and were deposited on a storm-influenced carbonate ramp. The overlying Svanbergfjellet Formation is subdivided into four informal members (lower dolostone, lower limestone, upper algal dolomite, and upper limestone; Knoll and Swett, 1990) and records the transition from a carbonate ramp to a rimmed carbonate platform. The Kinnvika Member, at the top of the Backlundtoppen Formation, contains abundant siltstone and mudstone and reflects a minor extensional episode (Halverson et al., 2018).

The BSA spans from the contact between the upper and lower members of the Grusdievbreen Formation to the contact between the lower dolomite and the lower limestone members of the Svanbergfjellet Formation (Fig. 2). Both of these contacts are subaerial exposure surfaces—the only two disconformities identified within the entire Akademikerbreen Group—and correspond with the nearly symmetric negative carbon isotope shifts of ~ 8‰ that define the BSA. The upper part of the lower member of the Grusdievbreen Formation comprises predominantly ribbon facies limestone (wavy laminated to fine-bedded calcilutite) with interbedded fine, tabular clast breccia, grainstone, and wackestone. However, in most sections, several meters of heavily recrystallized dolostone occur just below the exposure surface, and in one section, karst pipes filled with recrystallized dolostone extend some 20 m below the exposure surface (Halverson et al., 2007). Carbon isotope values drop from ~6‰ just below the surface to 0–1‰ in the lowermost carbonates of the upper member (Fig. 2). The lower part of this member consists of a visually distinct shoaling-upward parasequence, beginning with interbedded marly red siltstone and limestone with intraformational breccias and conglomerates, the clasts of which are commonly arranged in rosettes or imbricated. The remainder of the upper member of the Grusdievbreen Formation consists of non-descript, grey, recrystallized limestone inferred to be dominantly grainstone and microbialaminite facies. Early diagenetic talc occurs rarely but throughout the grey limestone (Halverson et al., 2007; Tosca et al., 2012) and is more abundant in the lower Svanberfjellet Formation (lower dolomite member), which comprises dolomitized, meter-scale, carbonate cycles deposited in an inner reef to back-reef setting (Halverson et al., 2018).

The end of the BSA corresponds to a second subaerial unconformity that defines the top of the lower dolomite member of the Svanberfjellet Formation, which is distinguished by heavy silicification, ferruginization, and local brecciation. The base of the overlying lower limestone member begins with green or black silty shale and grades upward into silty, wavy to parallel, medium-bedded limestone. This facies, in turn, transitions upward into a *Minjaria-Conophyton* biostrome that extends across the outcrop belt (Halverson et al., 2007; Knoll and Swett, 1990). The biostrome is succeeded by dominantly fine- to medium-bedded dark grey to black limestone (ribbon facies). $\delta^{13}C_{carb}$ rises sharply from a low of ~ -3‰ in the upper part of the lower dolomite member to > 6‰ in the grey and black limestones above the *Minjaria-Conophyton* biostrome in the overlying lower limestone member (Fig. 2).

In East Greenland, the base of the BSA corresponds to the upper contact of Bed-group 9 of the Ymer Ø Group (= Member 3 of the Brogetdal Formation; Fig. 3; Caby and Bertrand-Sarfati, 1988; Katz, 1961), which consists of blue-grey to grey, medium bedded limestone capped by a thin pale dolostone bed, the top of which is a subaerial unconformity (Fig. 4). The lower part of the overlying Bed-group 10 consists of green silt, grading upward into interbedded, thin and wavy pink and white limestone and dolomitic limestone beds and red, marly shale and silt. In the logged section on Ymer Ø (Fig. 4), this 22-m thick interval contains the BSA, and a sharp return to positive $\delta^{13}C_{carb}$ occurs in an overlying parasequence beginning with red shale with dolomitic layers that pass upwards into increasingly carbonate-rich, laminated to finely-bedded shaley limestone (ribbon facies). It is unclear why the BSA is so thin in this section; either it is highly condensed and not well represented due to the prevalence of silt and shale, or the section is incomplete due to missing strata on the disconformable surface separating Bed-groups 9 and 10.

2.2. Northwestern Canada

Early Neoproterozoic successions occur in Proterozoic inliers of the northern Canadian Cordillera. The Mackenzie Mountains Supergroup (MMSG) is a ~ 4-km-thick succession exposed in the Mackenzie Mountains, in western Northwest Territories, and in the Wernecke Mountains, in eastern Yukon (Fig. 5). The MMSG represents one part of a larger, interconnected, intracontinental basin in northwestern Canada that spanned much of the early Neoproterozoic and whose tectonic origin is debated (Aitken, 1981; Macdonald et al., 2013; Rainbird et al., 1996; Turner and Long, 2008). The best exposed and most studied units of the MMSG are the dominantly siliciclastic Katherine Group and the carbonate-dominated Little Dal Group, which is unconformably overlain in the northern Mackenzie Mountains by the Little Dal Basalt (Thorkelson et al., 2005). Here we focus on the Little Dal Group, in which Halverson (2006) documented the BSA. The Little Dal Group is loosely constrained to be younger than 1005 Ma based on U-Pb detrital zircons from the Katherine Group (Leslie, 2009), whereas a U-Pb zircon age of 775.10±0.54 Ma from a diabase within the Little Dal Basalt provides a minimum age (Milton et al, 2017).

The Little Dal Group consists of seven formations (Fig. 5). The basal Dodo Creek Formation records an initial transgression and is composed of fine-grained sandstone and mudstone with mudcracks at the base. The overlying Stone Knife

Formation was deposited on the basin margin with deep rhythmite facies and localized reefs. The Silverberry Formation is defined as the shallower facies equivalent to the Stone Knife Formation, consisting mainly of intraclastic and ooid grainstones. A stromatolite biostrome complex spatially separates the Stone Knife and Silverberry Formations. Next, the Gayna Formation is characterized by massive ooid grainstone and mudstone beds and secondary chert typical of an intertidal to supratidal environment. The Ten Stone Formation comprises a thick interval of gypsum (Aitken, 1981; Crockford et al., 2019; Turner and Bekker, 2016). The overlying Snail Spring Formation consists of mudstone with interbedded siltstone and quartz arenite overlain by laminated carbonates, all of which were deposited in a shallow marine environment. The Ram Head Formation at the top of the Little Dal Group includes abundant stromatolites and ooid grainstones deposited on a high-energy carbonate platform (Fig. 5; Aitken, 1981; Turner and Long, 2008; Turner and Long, 2012). In the northern part of the outcrop belt, the Ram Head Formation is unconformably overlain by the Little Dal Basalt.

Halverson (2006) first documented the BSA in the middle Ram Head Formation (formerly known informally as the Upper Carbonate) in a complete section of the Little Dal Group on the flank of Coppercap Mountain. In this section, the onset of the anomaly is marked by $\delta^{13}C_{carb}$ values dropping from +6‰ to -2‰ and occurs within a transgressive systems tract, recorded by a shift from wavy laminated dolostones below to rudstone debrites above. The anomaly spans ~175 m in section, and in contrast to Svalbard, the end of the anomaly, recorded in interbedded stromatolites and wavy dolostones, is gradual and is not associated with an exposure surface. In a new section (M304) measured near Stone Knife River (N004°38'1.49" W129°43'4.57"), the onset of the anomaly is abrupt and corresponds to a maximum flooding surface defined by the contact between lower wavy laminated dolo-grainstone beds with scour surfaces and ripples and maroon siltstone above. $\delta^{13}C_{carb}$ values decline from +7‰ to -2‰ (Halverson, 2006; Halverson et al., 2005). The end of the anomaly coincides with another maximum flooding surface highlighted by cherty microbialaminite dolostone beds overlain by black shales. The $\delta^{13}C_{carb}$ data then gradually rise back to pre-BSA values of ~ 6‰ (Fig. 6).

3. Methods

3.1. Sample selection

A total of 482 samples from 16 sections on northeastern Svalbard, 98 samples from one section in eastern Greenland, and 164 samples from one section in the Mackenzie Mountains, NWT (Table-1, supplementary information) were analyzed for this study. High-resolution sampling was conducted along multiple sections in Svalbard and all samples were collected in the context of broader stratigraphic studies. Samples were cut and drilled along single laminae or as clusters, with every effort made to avoid visible veining. This drilled powder was then used for the following analyses.

3.2. Carbon and oxygen isotopes

Carbon ($\delta^{13}C$) and oxygen ($\delta^{8}O$) stable isotopes were measured simultaneously in dual inlet mode on a Nu Instruments mass spectrometer coupled to a NuCarb automated carbonate preparation device in the Stable Isotope Laboratory at McGill University. Between 100-140 μg of rock powder was weighed out and then reacted with H_3PO_4 at 70°C, after which the CO_2 was cryogenically isolated. Isotopic ratios were measured against an in-house reference gas and calculated $\delta^{13}C$ and $\delta^{18}O$ values are reported on the V-PDB scale. The 1-σ uncertainty for $\delta^{13}C$ and $\delta^{18}O$ measurements is < 0.05‰ based on long-term analyses of NCM and UQ-6 standards.

3.3. Elemental concentrations

Concentrations of calcium, magnesium, iron, manganese and strontium (Ca, Mg, Fe, Mn and Sr) were acquired on a Thermo Scientific iCAP 6000 series Inductively Coupled Plasma Optical Emission Spectrometer (ICP-OES) at McGill University. Approximately 15 mg of sample powder was first washed with ultra-pure water and then dissolved in 2% nitric acid (HNO_3). The supernatant was then diluted in 2% HNO_3 for analysis on the ICP-OES. The Carbonatite-55 standard from the US Geological Survey was used as a quality control standard during each run. Final concentrations in the carbonate fraction were corrected for insoluble residue. The ICP-OES instrumental error is < 6% for Ca, < 2% for Mg, < 7% for Fe, < 4% for Mn and < 2% for Sr.

3.4. I/[Ca+Mg] ratios in carbonates

We adapted the I/Ca technique previously applied to Toarcian and Cenomanian-Turonian OAEs (Lu et al., 2010). Due to the abundance of dolomite in the Akademikerbreen Group, we have broadened this method to include both Mg and Ca in the denominator (I/[Ca+Mg]). Analyses were performed on 1-5 mg drilled powders, which were first dissolved in 3% HNO_3 and then diluted into solutions with a consistent matrix (50±5 ppm Ca). In order to stabilize iodine, 0.5% Tetramethylammonium hydroxide (TMAH) or tertiary amine was added. Furthermore, all solutions were analyzed within 2 hours of preparation to minimize loss of iodine (Lu et al., 2010; Tagami and Uchida, 2005). The I/[Ca+Mg] analyses were performed using a quadrupole ICP-MS (Bruker 90) at Syracuse University. The reference material used during the ICP-MS measurements is JCP-1 from the Geological Survey of Japan (Lu et al., 2010). Based on previous ICP-MS analyses, instrumental uncertainties are < 3% and the detection limit of I/Ca is on the order of 0.1 μmol/mol (Lu et al., 2010, 2017).

4. Results

We report I/[Ca+Mg], carbon and oxygen isotope, and elemental concentration data from carbonates spanning the BSA anomaly in Svalbard, East Greenland, and the Mackenzie Mountains. The I/[Ca+Mg] ratios from Svalbard and some new carbon and oxygen isotope data were previously published in Lu et al. (2017). The remaining carbon and oxygen isotope data from Svalbard were published in Halverson et al. (2005) and Halverson et al. (2018). All data ($\delta^{13}C_{carb}$, I/[Ca+Mg] and major elemental concentrations) from Greenland and Mackenzie Mountains, as well as all the carbonate major elemental concentrations from Svalbard, are presented here for the first time.

4.1. Svalbard

A total of 482 samples from the Akademikerbreen Group in Svalbard was used in this study, of which 349 samples were measured for I/[Ca+Mg] ratios, 383 for carbonate major elements, and 466 for carbon and oxygen isotopes (Table-1, supplementary information). The I/[Ca+Mg] ratios range from 0 to 7.69 μmol/mol with an average of 0.5 μmol/mol and a median of 0.19 μmol/mol, and carbon stable isotope data vary from +8‰ to -3‰. (Fig. 2).

Halverson et al. (2018b) applied a one-dimensional thermal subsidence model to calculate the sediment accumulation rates along the EGES carbonate platform in order to estimate the duration of $\delta^{13}C_{carb}$ shifts across the Tonian-Cryogenian transition. The first values of I/[Ca+Mg] distinctly above low background occur at a stratigraphic height of ~215 m (some 225 m below the onset of the BSA), corresponding to ca. 815 Ma. This increase coincides with a carbon isotope excursion (referred to hereafter as the pre-Bitter Springs Anomaly; Figs. 2-7) where $\delta^{13}C_{carb}$ drops from +8‰ to +2‰. The I/[Ca+Mg] values stay low at ~0.5 µmol/mol during this interval but spike to 1.48 µmol/mol during the recovery from the anomaly (Figs. 2-7; Table-1, supplementary information).

The coupled $\delta^{13}C_{carb}$ and I/[Ca+Mg] data define two distinct stages within the BSA. The early stage (stratigraphic height ~347–600 m) is characterized by I/[Ca+Mg] values lower than 1 µmol/mol coupled with $\delta^{13}C_{carb}$ declining from +8‰ to -1‰. A subsequent and subdued rise in $\delta^{13}C_{carb}$ up to +1‰ (~600 m) is followed by a second decline in $\delta^{13}C_{carb}$ values to as low as -3‰ and is associated with a spike in I/[Ca+Mg] ratios that includes the highest values in our dataset (up to 7.69 µmol/mol). This peak corresponds stratigraphically to the carbon isotope minimum and subsequent onset of the steep rise in $\delta^{13}C_{carb}$ back towards positive values at the end of the BSA (Figs. 2-7; Table-1, supplementary information). Above the BSA, I/[Ca+Mg] returns to the generally constant and low values (< 1 µmol/mol) that prevailed both prior to the onset of the BSA and in the middle of the BSA (Figs. 2-7).

4.2. East Greenland

A total of 98 samples from the Ymer Ø Group in East Greenland were analyzed for I/[Ca+Mg] ratios and 91 samples for carbonate major elemental analysis, combined with 93 carbon isotope measurements. Most of the strata recording the BSA are not exposed in East Greenland, and the exposed interval mostly records the time before and after the BSA along with the tail end of the anomaly (Figs. 4-7). The $\delta^{13}C_{carb}$ measurements still display the ~8‰ negative excursion characteristic of the BSA (Halverson et al. 2005, 2007). At the onset of the anomaly, carbon isotopic values decline from +6‰ to -2‰ and then rise back up to +6‰ at the end. I/[Ca+Mg] ratios span a relatively small range compared to the Akademikerbreen Group. These values extend from 0 µmol/mol to 1.77 µmol/mol with an average of 0.18 µmol/mol and a

median of 0.09 µmol/mol. Moreover, as observed in the Svalbard dataset, the highest I/[Ca+Mg] values of ~1.5 µmol/mol occur at the end of the BSA (Figs. 4-7; Table-1, supplementary information).

4.3. Northwest Canada

We measured 82 samples from the Mackenzie Mountains Supergroup in northwest Canada for I/[Ca+Mg], 162 for elemental concentrations and 164 for $\delta^{13}C_{carb}$. In our measured section, the BSA spans the upper Snail Spring Formation and the lower Ram Head Formation and records an ~8‰ negative shift (Figs. 6-7). The I/[Ca+Mg] values range from 0 to 0.91 µmol/mol with a total average of 0.08 µmol/mol and a median of 0.02 µmol/mol. The highest values at ~1 µmol/mol are observed in the few carbonates outcropping in the top of the Snail Spring Formation, corresponding to the small negative $\delta^{13}C$ excursion at ~140m beneath the onset of the BSA (Figs. 6-7; Table-1, supplementary information). This pre-BSA anomaly has the same amplitude as the one recorded on Svalbard (from +2‰ to +8‰; Figs. 2, 4 and 6). However, in contrast to Greenland and Svalbard, the I/[Ca+Mg] ratios stay close to 0 µmol/mol during the entire BSA (Figs. 6-7; Table-1, supplementary information).

5. Discussion

5.1. Preservation of primary I/[Ca+Mg] signatures

Based on a compilation of modern and ancient carbonates, Hardisty et al. (2017) showed that post-depositional alteration can affect I abundance in carbonates, and when it does, it typically decreases the ratio of I/[Ca+Mg]. Furthermore, authigenic carbonates do not incorporate iodate (IO_3^-) because they form under anoxic conditions where an iodate is completely reduced to iodide (I^-; Lu et al., 2017). Indeed, pore-water, near the water-sediment interface, is characterized by relatively high concentrations of iodide, regardless of the redox conditions of the overlying water. This zone of iodide production is the result of two processes. First, below the water-sediment interface, a near-closed cycle of iodine involves the remineralization of iodide from the breakdown of organic matter followed by rapid uptake by sediment particles. Hence, the decomposition of increasingly iodide-enriched organic matter results in elevated iodine concentrations in unlithified sediments. Second, in deeper layers, iodate reduction occurs under suboxic conditions. The relatively high flux of

iodide is associated with the burial of organic material and subsequent diagenetic recycling (Kennedy and Elderfield, 1987). This iodide cannot be incorporated into carbonate minerals, but rather diffuses back to seawater, and thus this burial reflux of iodide does not influence the ratio of I/[Ca+Mg] measured in marine carbonate. Therefore, measured I/[Ca+Mg] in ancient carbonates provides a minimum constraint on local seawater iodate abundance, and high I/[Ca+Mg] ratios are inferred to record high iodate abundance in the waters in which the carbonates were precipitated. In contrast, since early or late diagenetic processes tend to reduce I/[Ca+Mg] ratios (Ahm et al., 2018; Hardisty et al., 2017), low ratios alone cannot be used to argue for low local seawater iodate abundance.

One process theoretically able to modify the I/[Ca+Mg] signal independently of local oxygen conditions is evaporation in restricted environments, where precipitation of $CaSO_4$ decreases the amount of Ca of ambient seawater independent of changes in iodate abundance. Moreover, brines tend to be enriched in iodide (Collins et al., 1969). However, the stratigraphic intervals studied here do not contain any evaporitic minerals or relict indicators of evaporative conditions, despite widespread occurrence of sulfate evaporites in middle Tonian basins (Turner and Bekker, 2016). Therefore, we conclude that evaporation did not strongly influence I/[Ca+Mg] on the Akademikerbreen carbonate platform. Nevertheless, in order to evaluate possible impacts of local restriction on I/[Ca+Mg] ratios as well as other processes such as meteoric diagenesis and dolomitization, we compare geochemical parameters that might indicate local modification of seawater or post-depositional resetting of sedimentary signatures.

A cross-plot of I/[Ca+Mg] versus Mg/Ca (Fig. 8a) clearly shows bimodal populations corresponding to calcite-dominated (Mg/Ca < 0.2) and dolomite-dominated (Mg/Ca > 0.4) carbonates. Greenland samples are mostly composed of calcite whereas the carbonates from the section in the Mackenzie Mountains are almost exclusively dolomite. Samples from Svalbard are a mixture of both calcite and dolomite with no clear correlation with I/[Ca+Mg] ratios, suggesting that dolomitization was not able to lower I/[Ca+Mg] ratios to levels observed in NW Canada. Additionally, in samples from East Greenland and from Svalbard, the $\delta^{18}O$ of calcites is almost entirely between -6 and -12‰, and dolomites are slightly enriched (Fig. 8f). These relatively heavy values suggest that dolomitization occurred during early diagenesis, (Halverson et al., 2007), consistent with excellent preservation of

primary sedimentary fabrics. In contrast, carbonate $\delta^{18}O$ values from the Mackenzie Mountains, composed mostly of dolomite are lower on average (-3 to -12‰). But regardless of dolomite abundance, there is a clear difference between $\delta^{18}O$ values measured in dolomite and values in calcite, with dolomite values ranging from -3‰ to -7‰ and calcite values ranging from -9‰ to -12‰ (Fig. 8f). These overall more depleted values in the Mackenzie Mountains suggest that dolomitization occurred after the calcites were first subjected to meteoric diagenesis. This inference is consistent with more extensive and coarser recrystallization, obliteration of primary textures, and elemental signatures within these samples.

During meteoric diagenesis, strontium (Sr) content in the carbonate typically decrease while manganese (Mn) and iron (Fe) increase (Brand and Viezer, 1980). Most of the samples from Svalbard and East Greenland display evidence of only limited meteoric diagenetic alteration, with Mn/Sr ratios rarely exceeding ~ 2-3 (Figs. 8b-c-f; Brand and Veizer, 1980). The effect of meteoric diagenesis on I/[Ca+Mg] ratios is most apparent when I/[Ca+Mg] is plotted against Mn/Sr: the highest I/[Ca+Mg] ratios occur in samples with Mn/Sr < 2 (Fig. 8b). This pattern suggests that post-depositional alteration likely lowered I/[Ca+Mg] ratios to variable degrees in our samples. On the other hand, samples with very high Sr contents do not invariably preserve higher I/[Ca+Mg] ratios, indicating that some low I/[Ca+Mg] ratios in these rocks may be primary seawater signatures. Our data are consistent with the argument that diagenesis results in increased variability in I/[Ca+Mg] and generally lower values, but cannot account for high I/[Ca+Mg] (Hardisty et al, 2017; Lu et al., 2018).

Samples from the Mackenzie Mountains are typically enriched in Fe (Fig. 8d) and have low Sr concentrations (close to the detection limit; Fig. 8c), as well as universally low I/[Ca+Mg] ratios. Enrichment of Fe coupled with a depletion of Sr is a common consequence of both diagenetic alteration due to equilibration with meteoric water and dolomitization (Brand and Veizer, 1980). These combined geochemical and sedimentological observations suggest that Mackenzie Mountains samples experienced a much higher degree of alteration during diagenesis (meteoric alternation followed by dolomitization) compared to the EGES samples. Based on these diagenetic considerations, we interpret the I/[Ca+Mg] ratios from the Mackenzie Mountains samples to record complete removal of any available iodate during recrystallization and dolomitization.

5.2. Interpreting the linked $\delta^{13}C_{carb}$ and I/[Ca+Mg] records

In the modern environment, under oxic conditions, iodine follows a nutrient-type profile in the water column. In the photic zone, phytoplankton take up iodate during photosynthesis and fix it as iodide in organic matter. At depth, the concentration of iodate slowly recovers and reaches a maximum at the OMZ as a result of organic matter remineralization. Below the OMZ, iodate concentrations are generally invariant. A flux of iodine also exists from bottom waters to ocean sediments (Tsunogai, 1971; Tsunogai and Henmi, 1971). In oxygenated waters, iodate does not track oxygen concentrations because iodate is controlled by productivity and incorporation into organic matter (Campos et al., 1996; Elderfield and Truesdale, 1980; Jickells et al., 1988; Tsunogai and Sase, 1969; Wong and Brewer, 1974). On the other hand, where oxygen concentration decreases to zero, as in some OMZs or anoxic deep waters, iodate will track the decrease in oxygen abundance. Under anoxic conditions, iodide effectively becomes the only iodine species. The increase in iodide under these conditions reflects the chemical reduction of iodate along with input from remineralized organic matter (Luther and Campbell, 1991; Luther and Cole, 1988; Wong and Brewer, 1976).

The removal of iodine from the upper ocean is largely attributed to the effects of biological uptake during photosynthesis. In highly productive upwelling zones in the modern ocean, iodate concentrations are low relative to less productive regions (Cutter et al., 2018; Truesdale and Bailey, 2000). At the same time, O_2 concentrations are elevated due to photosynthesis. Therefore, even though total iodate abundance in the oceans is linked to oxygen content, locally, iodate depletion, i.e. low I/[Ca+Mg] may reflect high primary productivity rather than O_2-depleted waters (Truesdale et al., 2000; Truesdale and Bailey, 2000).

5.2.1. The Svalbard–East Greenland record and implications for the BSA

Most of our samples spanning the BSA have non-zero I/[Ca+Mg] values implying the presence of iodate in our carbonates incorporate from seawater (Figs. 2, 4, 6 and 7). Proterozoic I/[Ca+Mg] ratios are lower than modern values, a consequence of lower iodate concentrations in seawater, rather than a smaller total dissolved iodine pool in the ocean at that time (Hardisty et al., 2017). Furthermore, late stage dolomitization reduces the ratio of I/[Ca+Mg] in primary carbonate phases (Loope et al., 2013). Therefore, the I/[Ca+Mg] ratio in dolostones provides only a minimum

estimate of iodate content in seawater at the time of initial carbonate precipitation (Hardisty et al., 2017). Intense meteoric alteration and authigenic carbonate formation (Lu et al., 2017) will result in low I/[Ca+Mg] ratios that are not indicative of seawater. Conversely, because no secondary processes are known to increase the I/[Ca+Mg] ratio in carbonate minerals, high ratios most likely represent primary seawater signatures.

The dolostones from the Akademikerbreen Group analyzed in this study were deposited on a shallow carbonate platform prone to early dolomitization (Knoll and Swett, 1990). Accordingly, the presence of iodine in these Neoproterozoic dolomites can be considered to be a qualitative proxy for the redox state of shallow waters (Hardisty et al., 2014, 2017). Combining this redox-proxy with $\delta^{13}C_{carb}$ provides the opportunity to better interpret the redox conditions of shallow marine environments spanning the BSA (Figs. 2, 4, 6 and 7).

Based on various paleobiological and geochemical data and inferences, it has been suggested that the late Mesoproterozoic to early Neoproterozoic (ca. 1.2–0.8 Ga) saw a gradual change in Earth's biosphere (Butterfield, 2000, 2001; Crockford et al., 2019; Knoll et al., 2013) coupled to a rise in atmospheric oxygen levels (Cole et al., 2016; Gilleaudeau et al., 2016; Planavsky et al., 2014). This hypothesis is consistent with the canonical interpretation linking $\delta^{13}C_{carb}$ with organic carbon burial and net release of O_2 to the environment because average $\delta^{13}C_{carb}$ values increase from ~0‰ to > +5‰ over this time interval (Des Marais, 1997; Des Marais et al., 1992; Kah et al., 2001; Kah et al., 1999; Knoll et al., 1986). It is also consistent with the occurrence of significant sulfate evaporite deposits in the ca. 1.05 Ga Angmaat Formation (Gibson et al., 2017a,b; Kah et al., 2001) of the Bylot Supergroup and the ca. 850–830 Ma Minto Inlet Formation in the Shaler Supergroup and the Ten Stone Formation in the Mackenzie Mountain Supergroup, along with similar-aged rocks globally (Crockford et al., 2019; Prince et al., 2019; Turner and Bekker, 2016). These widespread evaporites are interpreted to indicate at least a transient pulse in oxidative weathering and growth of the marine sulfate reservoir in the middle Tonian (Kah et al., 2001; Kah et al., 2004; Turner and Bekker, 2016), although widespread evaporate deposition in intracratonic basins at this time likely drew concentrations down again (Prince et al., 2019). Furthermore, eukaryotic diversity appears to have risen sharply by ca. 800 Ma (Cohen and Macdonald, 2015; Riedman and Sadler, 2017). On the other hand, previous

redox studies exploring the late Mesoproterozoic to early Neoproterozoic (1200–717 Ma) ocean suggest that oxygenated shallow waters overlay predominantly ferruginous deep waters (Fe^{2+}-rich and anoxic), perhaps temporally or spatially punctuated by periods of euxinia (sulfidic and anoxic) localized in mid-shelf environments (Canfield et al., 2008; Guilbaud et al., 2015; Johnston et al., 2010; Poulton et al., 2010; Sperling et al., 2013; Sperling et al., 2015). Kunzmann et al. (2015) concluded that non-BSA Tonian to Ediacaran samples accumulated beneath suboxic to anoxic-ferruginous water columns based on a multi-proxy study of black shales from the Akademikerbreen and Polarisbreen groups.

The generally low I/[Ca+Mg] ratios leading up to the onset of the Bitter Springs Anomaly in Svalbard are consistent with a generally anoxic, stable deep ocean (Fig. 9). Such redox conditions would be expected to enhance phosphorus (P) scavenging through a combination of different Fe-P trap processes (Bjerrum and Canfield, 2002; Derry, 2015; Jones et al., 2015; Reinhard et al., 2017; Sundby, 2006; Zegeye et al., 2012). On the other hand, even though phosphorus was most likely the limiting nutrient on primary productivity at this time (Anbar and Knoll, 2002; Reinhard et al., 2017), the heavy coeval $\delta^{13}C_{carb}$ values may indicate sustained high rates of organic carbon burial, evidently requiring high nutrient availability, even if certain cyanobacteria can be flexible in their C:N:P uptake ratio (White et al., 2006; White, 2009). Enhanced weathering of continental flood basalts at this time may have contributed to elevated P supply (Cox et al., 2016; Horton, 2015).

The negative shift in $\delta^{13}C_{carb}$ defining the beginning of the BSA is gradual and does not result in a decline to a distinct minimum, as is typical of other Neoproterozoic negative $\delta^{13}C_{carb}$ anomalies (Halverson et al., 2005). Assuming that the carbon isotope signature in carbonates records the global DIC reservoir, this distinction suggests that the driving mechanism was not a non-steady perturbation driven by addition of isotopically depleted carbon, but rather a change in the fraction of organic carbon burial (f_{org}). In Svalbard, this shift corresponds with an exposure surface (Fig. 2); in northwestern Canada (Fig. 6; Halverson, 2006) and in central Australia it is associated with transgression (Swanson-Hysell et al., 2010). The implication is that both the decline in organic burial and base level fluctuations were linked to global oceanographic phenomena (Maloof et al., 2006).

A small, short-lived spike in I/[Ca+Mg] at the boundary is consistent with this hypothesis and can be explained in terms of transfer of iodine from the reduced iodide

reservoir to the oxidized iodate reservoir related to a reorganization of ocean circulation rather than a pulse in oxygenation of the oceans. Maloof et al. (2006) proposed an episode of true polar wander (TPW) at this time to explain the onset of the BSA, but even more subtle changes in paleogeography coupled to early rifting of Rodinia could easily have temporarily changed patterns of ocean circulation and upwelling zones. Based on abundant sulfate evaporites deposited in intracratonic basins just prior to the BSA (Crockford et al., 2019; Hill et al., 2000; Prince et al., 2019; Turner and Bekker, 2016) one can infer that marine sulfate concentrations were relatively high at this time (at least compared to the mid-Proterozoic).

The early BSA stage is characterized by I/[Ca+Mg] ratios under 2.5μmol/mol, a commonly assumed threshold for O_2-depleted ocean condition such as found in modern OMZs (Lu et al., 2017; Lu et al., 2016; Lu et al., 2010). At the onset of the BSA, high sulfate availability combined with anoxic deepwaters, promoted the expansion of euxinic conditions in upwelling zones capable of sustaining high productivity. Indeed, nutrient-rich deep waters are necessary to sustain the expansion of deep euxinic conditions (Fig. 9; Lyons et al., 2014; Reinhard et al., 2016). In the Shaler Supergroup (Amundsen Basin) of northern Canada, the base of the Bitter Springs Anomaly corresponds to a shift from anoxic ferruginous to euxinic deep waters and the accumulation of organic-rich shales (Thomson et al., 2015). Carbonates from this interval, which have virtually no I, do not reflect surface seawater because they formed authigenically in organic-rich sediments (Lu et al., 2017). The low I/[Ca+Mg] recorded in coeval shallow marine carbonates on EGES platform (Figs. 2 and 4) can be interpreted in terms of efficient iodate removal from the photic zone by phytoplankton rather than global O_2-depletion in seawater.

Widespread euxinic conditions would have been sufficient to draw down certain trace metal inventories, most importantly, molybdenum (Reinhard et al., 2013). Low Mo supply in seawater would also inhibit nitrogen-fixing cyanobacteria due to the dependence of some nitrogenases on molybdenum (Latysheva et al., 2012; Williams and Da Silva, 2002), resulting in coupled Mo-N co-limitation on primary productivity rather than P-limitation. Such a scenario of euxinia-driven nutrient limitation likely prevailed through much of the Paleoproterozoic and Mesoproterozoic (2500–1200 Ma) and may have accounted for limited primary production at this time (Anbar and Knoll,

2002; Crockford et al., 2018; Falkowski, 1997; Saito et al., 2003) with a long-lived average $\delta^{13}C_{carb}$ values near 0‰ (e.g., Buick et al., 1995). It is unlikely a coincidence that the BSA, like the Paleoproterozoic and Mesoproterozoic, is characterized by stable $\delta^{13}C_{carb}$ values near 0‰ and correspondingly low f_{org} (Halverson et al., 2005), and it follows that the fundamental limit on organic carbon burial during the BSA may have similarly been related to Mo-N limitation on primary productivity resulting from expanded deepwater euxinia (Fig. 9). Moreover, diminishing the iodine sink in organic matter (Luther and Campbell, 1990; Luther and Cole, 1988; Wong and Brewer, 1976) by lowering primary production during the last stage of the BSA would allow iodide to accumulate in a euxinic deep ocean (Fig. 9).

The recovery from the BSA is virtually a mirror image of the anomaly's onset, although in Svalbard, $\delta^{13}C_{carb}$ values first decline to a minimum prior to the steady rise back to positive values. This positive shift is also associated with another subaerial exposure surface followed by a rapid transgression in Svalbard (Fig. 2; Halverson et al., 2007) and an abrupt change in facies in central Australia (Swanson-Hysell et al., 2010). However, distinct from the onset of the BSA, the response in I/[Ca+Mg] is much more pronounced, with a peak of > 7 μmol/mol—the highest I/[Ca+Mg] values yet recorded between the ca. 2.2 Ga Lomagundi positive isotope excursion and the ca. 570 Ma Shuram negative carbon isotope anomaly (Lu et al., 2017). Furthermore, the shift to high I/[Ca+Mg] values occurs well below the exit from the BSA and is recorded within the entirely dolomitic lower dolomite member of the basal Svanberfjellet Formation, which displays no change in depositional facies. Interestingly, the increase in I/[Ca+Mg] coincides with the onset of a downturn towards more negative $\delta^{13}C_{carb}$ values prior to recovery from the BSA, and the peak coincides with the minimum (Fig. 2) and onset of a return to positive values. The I/[Ca+Mg] peak is relatively short-lived, with ratios returning to average values < 0.1 μmol/mol afterwards. This pattern might record a net transfer of iodine from the iodide reservoir, which accumulated over the course of the BSA, to the iodate reservoir, rather than a unique 'oxidation event' (although sufficient oxygen must have been available in the surface ocean to facilitate its oxidation; Fig. 9). The subsequent and sharp return to the highly positive $\delta^{13}C_{carb}$ therefore indicates that the nutrient barrier to primary production was removed, presumably due to a contraction of the global extent of euxinia. Combined with high background P concentrations (Fig. 9; Cox et al., 2016;

Planavsky et al., 2010), this expansion in Mo inventory sustained a return to high primary productivity and organic carbon burial (Crockford et al., 2019).

Another smaller excursion in $\delta^{13}C_{carb}$ occurs in the lower Grusdievbreen Formation, where like the end BSA peak, it is associated with a positive isotopic shift following lower $\delta^{13}C_{carb}$ values (i.e., the pre-Bitter Springs anomaly; Figs. 2-6). A negative correlation between lower $\delta^{13}C_{carb}$ values and higher I/[Ca+Mg] values in this pre-BSA excursion is identical to that at the end of the BSA (Fig. 2). It suggests that these patterns are primary seawater signals and related to paleoceanographic changes that enhanced nutrient availability while shuffling iodide to the oxygenated surface ocean. Consequently, taken as a whole, the I/[Ca+Mg] record is consistent with a scenario in which Tonian marine waters were generally anoxic beneath an oxygenated surface mixed layer with phosphorus limiting primary productivity (albeit at high f_{org}), but the BSA and perhaps some smaller $\delta^{13}C_{carb}$ anomalies point to times of expanded euxinia and Mo-N limitation. This interpretation suggests that while the high I/[Ca+Mg] values at the end of the BSA likely indicate surface seawater oxygen contents that were higher than at any time in the preceding 1.2 billion years (Blättler et al., 2018), they do not signify sustained whole ocean oxygenation, for example as suggested by consistently high I/[Ca+Mg] values in the Phanerozoic record (Lu et al., 2018).

5.2.2. The BSA as recorded in the Little Dal Group (Mackenzie Mountains, NWT)

The Bitter Springs Anomaly has been documented in multiple sections of the Little Dal Group in the Mackenzie Mountains (Fig. 6; Halverson, 2006) and in the equivalent strata in the Fifteenmile Group of Yukon (Macdonald et al., 2010; Macdonald et al., 2013). However, I/[Ca+Mg] ratios from our analyzed section of the Little Dal Group spanning the BSA only show a flat-line trend of values < 0.5 µmol/mol. The heavily recrystallized carbonate textures, along with geochemical data (high Mn/Sr ratios and an offset in $\delta^{18}O$ data between calcites and dolomites (Fig. 8), indicate a high degree of alteration as a result of meteoric diagenesis followed by late stage dolomitization. Consequently, we infer that while carbon isotope ratios were resilient, primary seawater I/[Ca+Mg] signatures were essentially obliterated, with the exception of a few non-zero I/[Ca+Mg] values from within the Snail Spring Formation (Fig. 6). Diagenetic stabilization of the dolomite samples preserving positive

I/[Ca+Mg] ratios may have been early enough to retain a portion of the primary oxygenated seawater signature, suggesting diagenesis under heavily fluid-buffered conditions or in equilibrium with a well-oxygenated diagenetic fluid that could have oxidized iodide to iodate. The Little Dal data justify caution in interpreting low I/[Ca+Mg] ratios in pervasively dolomitized carbonates in terms of seawater conditions. That is, secular variations in I/[Ca+Mg] through time, especially through the Precambrian are potentially more a record of alteration than changes to surface oxygenation. At the same time, when comparing samples from the Mackenzie Mountains with samples from Svalbard, which preserve I/[Ca+Mg] enrichments, these data highlight the importance of the relative timing of dolomitization in at least partially preserving primary seawater signatures. Furthermore, these data demonstrate that carbon isotope ratios in thick, carbonate-dominated successions can be well buffered against wholesale resetting.

5.3. A conceptual model for the BSA

The Tonian period witnessed an increase in average $\delta^{13}C_{carb}$ from the near 0‰ values that prevailed through much of the late Paleoproterozoic and Mesoproterozoic to values > 5‰, which characterize much of the Neoproterozoic Era. If we assume that these high average $\delta^{13}C_{carb}$ values reflect high f_{org}, then they must imply high nutrient availability. We have developed the hypothesis that the Bitter Springs Anomaly records a temporary (ca. 8 m.y.) reversion to the earlier, mid-Proterozoic-like stable state in global carbon cycling. In this scenario, the near zero to slightly negative $\delta^{13}C_{carb}$ during the BSA reflect Mo-N limitation on primary productivity resulting from sufficiently expansive euxinic conditions to drawdown the seawater molybdate reservoir and stifle nitrogen fixation. This hypothesis requires the assumption that alternative nitrogenases (Robson et al., 1986; Zhang et al., 2014) were either not significant in fixing nitrogen at this time or unable to compensate for Mo-N limitation (Fig. 9).

The return to high $\delta^{13}C_{carb}$ values at the end of the BSA is linked to a short-lived peak in I/[Ca+Mg] ratios that must signify an oceanographic phenomenon which transferred iodide from the deep ocean to the oxidized iodate reservoir, allowing it to be incorporated in shallow-water carbonates. At the same time, the Mo-N limitation was alleviated, and the stable carbon cycle state shifted to one in which primary productivity was limited by P (Fig. 9). Whether or not the late BSA I/[Ca+Mg] peak

was a global seawater phenomenon or limited to continental platforms influence by upwelling, such as Svalbard-East Greenland, remains to be tested by additional data from other Tonian successions.

The stratigraphic record links the onset and end of the BSA to eustatic fluctuations in sea level. But what drove these oceanographic changes? Based on the stratigraphic context of the BSA, along with paleomagnetic data from Svalbard, Maloof et al. (2006) proposed that the onset and end of the BSA were related to largescale true polar wander (TPW), during which the silicate earth first rotated some 55º relative to the spin axis, and then back by approximately the same magnitude, each over a time scale of millions of years. Such an oscillatory geodynamic process, while extraordinary compared to the much more subtle TPW that accompanies the growth and decay of ice sheets (Milne and Mitrovica, 1996; Mitrovica and Milne, 1998) and more recent advection of mantle heterogeneities (Steinberger and O'Connell, 1997), is however physically viable (e.g., Creveling et al., 2012; Evans, 1998; Gold, 1955; Kirschvink et al., 1997; Matsuyama et al., 2006). The suggested TPW event is predicted to generate large fluctuations in sea level (Mound et al., 1999) and would be anticipated to elicit wholesale reorganization of ocean circulation. Furthermore, modest but still significant (~30º) oscillatory TPW is thought to have occurred during the Mesozoic (Muttoni et al., 2013). The hypothesis that the BSA is linked to a pair of TPW events remains viable but has not been validated by paleomagnetic data from any other sedimentary basin (Swanson-Hysell et al., 2012). However, even in the absence of large scale TPW at this time, the early stages of onset of Rodinia break-up (Li et al., 2013) could similarly have elicited massive changes to ocean circulation, just as plate tectonic events related to break-up of Pangaea dramatically perturbed ocean circulation, nutrient delivery, and global climate (e.g., Elsworth et al., 2017; Kennet, 1977; Yang et al., 2013). While inevitably speculative, it is reasonable to assume that reorganization of upwelling and marine nutrient cycling in a dominantly anoxic ocean would have had profound biogeochemical responses.

6. Conclusions

Regardless of the precise trigger mechanism for the BSA, our coupled I/[Ca+Mg] and $\delta^{13}C_{carb}$ datasets from multiple sedimentary successions spanning the BSA yield several firm conclusions. First, although the I/[Ca+Mg] proxy is clearly

prone to overprinting and should be treated only as a minimum estimate for surface seawater values, it can be a valuable tool in inferring ancient changes in the redox chemistry of local basins or margins and possibly the global ocean. Second, carbonates from within the BSA record some of the highest I/[Ca+Mg] in the Precambrian, including peak values (> 6 μmol/mol) that are comparable to modern marine carbonates (Hardisty et al., 2017; Lu et al., 2017). However, these high values are not sustained and presumably reflect a reorganization of the iodine pool in seawater and not an oxygenation event *per se*. On the other hand, they must reflect sufficiently high oxygen contents in the surface mixed layer to readily oxidize this iodide. Third, positive excursions in I/[Ca+Mg] are closely linked to sharp positive shifts in $\delta^{13}C_{carb}$, indicating a close link between these anomalies and global carbon cycling. We further hypothesize that the high $\delta^{13}C_{carb}$ characterizing much of the Neoproterozoic Era reflects an ocean with dominantly anoxic but not euxinic deepwaters in which primary productivity was limited by P, whereas the BSA records a temporary shift to more euxinic oceans where primary productivity was curtailed by low Mo and fixed nitrogen (Fig. 9). The limited iron speciation data available for the Tonian period are consistent with this hypothesis (Kunzmann et al., 2015; Sperling et al., 2013, 2015; Thomson et al., 2015), but it should be further tested with additional redox proxy data. Although the BSA is closely related in time to proposed oxygenation (Cole et al., 2016; Planavsky et al., 2014) and eukaryotic diversification (Cohen and Macdonald, 2015) events and appears to reflect the broad evolution of atmospheric and ocean redox, its ultimate cause may be more closely related to changing Tonian paleogeography then secular change in the marine oxygen inventory.

Acknowledgements

This manuscript was greatly improved following reviews by D. Hardisty and J. Husson. We acknowledge Isabelle Richer for the help with the analyses at McGill University. We thank Zunli Lu, Xiaoli Zhou and Wanyi Lu for discussions and laboratory analyses undertaken at Syracuse University. SW acknowledges support from McGill University. PWC acknowledges funding from an NSERC-CREATE through Boswell A. Wing, as well as the Agouron Institute Postdoctoral Fellowship program. MK is grateful for various graduate student fellowships from McGill

University and GEOTOP. This project was partially supported by NSERC Discovery grants to GPH.

References

Ahm, A.S.C., Bjerrum, C.J., Blättler, C.L., Swart, P.K., Higgins, J.A., 2018. Quantifying early marine diagenesis in shallow-water carbonate sediments. Geochimica et Cosmochimica Acta. doi: 10.1016/j.gca.2018.02.042

Aitken, J.D., 1981. Stratigraphy and sedimentology of the Upper Proterozoic Little Dal Group, Mackenzie Mountains, Northwest Territories. Proterozoic basins of Canada: Geological Survey of Canada Paper, 81(10), 47-71.

Aitken, J.D., Long, D.G.F., 1978. Mackenzie tectonic arc-reflection of early basin configuration? Geology, 6 (10), 626-629. doi: 10.1130/0091-71613(1978)

Anbar, A.D., Knoll, A.H., 2002. Proterozoic ocean chemistry and evolution: a bioinorganic bridge? Science, 297 (5584), 1137-1142. doi: 10.1126/science.1069651

Banner, J.L., 1995. Application of the trace element and isotope geochemistry of strontium to studies of carbonate diagenesis. Sedimentology, 42 (5), 805-824. doi: 10.1111/j.1365-3091.1995.tb00410.x

Bjerrum, C.J., Canfield, D.E., 2002. Ocean productivity before about 1.9 Gyr ago limited by phosphorus adsorption onto iron oxides. Nature, 417 (6885), 159-162. doi: 10.1038/417159a

Blättler, C.L., Claire, M.W., Prave, A.R., Kirsimäe, K., Higgins, J.A., Medvedev, P., Romashkin, A.E., Rychanchik, D.V., Zerkle, A.L., Paiste, K., Kreitsmann, T., Millar, I.L., Hayles, J.A., Bao, H., Turchyn, A.V., Warke, M.R., Lepland, A., 2018. Two-billion-year-old evaporites capture Earth's great oxidation. Science, 360 (6386), 320-323. doi: 10.1126/science.aar2687

Brand, U., Veizer, J., 1980. Chemical diagenesis of a multicomponent carbonate system-1: Trace elements. Journal of Sedimentary Research, 50 (4), 1219-1236.

Brocks, J.J., Jarrett, A.J., Sirantoine, E., Hallmann, C., Hoshino, Y., Liyanage, T., 2017. The rise of algae in Cryogenian oceans and the emergence of animals. Nature, 548 (7669), 578-581. dio: 10.1038/nature23457

Buick, R., Des Marais, D.J., Knoll, A.H., 1995. Stable isotopic compositions of carbonates from the Mesoproterozoic Bangemall Group, northwestern Australia. Chemical Geology, 123 (1-4), 153-171. doi: 10.1016/0009-2541(95)00049-R

Butterfield, N.J., 2000. *Bangiomorpha pubescens* n. gen., n. sp.: implications for the evolution of sex, multicellularity, and the Mesoproterozoic/Neoproterozoic radiation of eukaryotes. Paleobiology, 26 (3), 386-404. doi: 10.1666/0094-8373(2000)026

Butterfield, N.J., 2001. Paleobiology of the late Mesoproterozoic (ca. 1200 ma) hunting formation, Somerset Island, Arctic Canada. Precambrian Research, 111 (1), 235-256. doi: 10.1016/S0301-9268(01)00162-0

Butterfield, N.J., 2009. Oxygen, animals and oceanic ventilation: an alternative view. Geobiology, 7 (1), 1-7. doi: 10.1111/j.1472-4669.2009.00188.x

Caby, R., Bertrand-Sarfati, J., 1988. The Eleonore Bay Group (central East Greenland). Later Proterozoic Stratigraphy of the Northern Atlantic regions, 212-236.

Campos, M.L.A.M., Farrenkopf, A.M., Jickells, T.D., Luther Iii, G.W.,1996. A comparison of dissolved iodine cycling at the Bermuda Atlantic Time-series Station and Hawaii Ocean Time-series Station. Deep Sea Research Part II: Topical Studies in Oceanography, 43 (2-3), 455-466. doi: 10.1016/0967-0645(95)00100-X

Canfield, D.E., 1998. A new model for Proterozoic ocean chemistry. Nature, 396 (6710), 450-453. doi: 10.1038/24839

Canfield, D.E., Poulton, S.W., Knoll, A.H., Narbonne, G.M., Ross, G., Goldberg, T., Strauss, H., 2008. Ferruginous conditions dominated later Neoproterozoic deep-water chemistry. Science, 321 (5891), 949-952. doi: 10.1126/science.1154499

Canfield, D.E., Poulton, S.W., Narbonne, G.M., 2007. Late-Neoproterozoic deep-ocean oxygenation and the rise of animal life. Science, 315 (5808), 92-95. doi: 10.1126/sicence.1135013

Canfield, D.E., Teske, A., 1996. Late Proterozoic rise in atmospheric oxygen concentration inferred from phylogenetic and sulphur-isotope studies. Nature, 382 (6587), 127. doi: 10.1038/382127a0

Cohen, P.A., Macdonald, F.A., 2015. The Proterozoic record of eukaryotes. Paleobiology, 41 (4), 610-632. doi: 10.1017/pab.2015.25

Cole, D.B., Reinhard, C.T., Wang, X., Gueguen, B., Halverson, G.P., Gibson, T.M., Hodgskiss, S.W.M., McKenzie, R.N., Lyons, T.W., Planavsky, N.J., 2016. A shale-hosted Cr isotope record of low atmospheric oxygen during the Proterozoic. Geology, 44 (7), 555-558. doi: 10.1130/G37787.1

Collins, A.G., 1969. Chemistry of some Anadarko basin brines containing high concentrations of iodide. Chemical Geology, 4 (1-2), 169-187. doi: 10.1016/0009-2541(69)90044-8

Cox, G.M., Halverson, G.P., Stevenson, R.K., Vokaty, M., Poirier, A., Kunzmann, M., Li. Z.X., Denyszyn. S.W., Staruss. J.V., Macdonald, F.A., 2016. Continental flood

basalt weathering as a trigger for Neoproterozoic Snowball Earth. Earth and Planetary Science Letters, 446, 89-99. doi: 10.1016/j.epsl.2016.04.016

Creveling, J.R., Mitrovica, J.X., Chan, N.H., Latychev, K., Matsuyama, I., 2012. Mechanisms for oscillatory true polar wander. Nature, 491(7423), 244. doi: 10.1038/nature11571

Crockford, P.W., Hayles, J.A., Bao, H., Planavsky, N.J., Bekker, A., Bui, T.H., Halverson, G.P., Frallick, P., Peng, Y., Wing, B.A., (2018). Triple Oxygen Isotope Evidence for Limited mid-Proterozoic primary production. Nature, 559, 613-616. doi: 10.1038/s41586-018-0349-y

Crockford, P.W., Kunzmann, M., Bekker, A., Hayles, J., Bao, H., Halverson, G.P., Peng, Y., Bui, T.H., Cox, G.M., Gibson, T.M., Wörndle, S., Rainbird, R., Lepland, A., Swanson-Hysell. N.L., Master, S., Sreenivas, B., Kuznetsov, A., Krupenik, V., Wing, B.A. (2019). Claypool continued: Extending the isotopic record of sedimentary sulfate. Chemical Geology, 513, 200-225. doi: 10.1016/j.chemgeo.2019-02-030

Cutter, G.A., Moffett, J.G., Nielsdóttir, M.C., Sanial, V., 2018. Multiple oxidation state trace elements in suboxic waters off Peru: In situ redox processes and advective/diffusive horizontal transport. Marine Chemistry, 201, 77-89. doi: 10.1016/j.marchem.2018.01.003

Derry, L.A., 2015. Causes and consequences of mid-Proterozoic anoxia. Geophysical Research Letters, 42 (20), 8538-8546. doi: 10.1002/2015GL065333

Des Marais, D.J., 1997. Isotopic evolution of the biogeochemical carbon cycle during the Proterozoic Eon. Organic Geochemistry, 27 (5), 185-193. doi: 10.106/S0146-6380(97)00061-2

Des Marais, D.J., Strauss, H., Summons, R.E., Hayes, J.M., 1992. Carbon isotope evidence for the stepwise oxidation of the Proterozoic environment. Nature, 359 (6396), 605-609. doi: 10.1038/359605a0

Elderfield, H., Truesdale, V.W., 1980. On the biophilic nature of iodine in seawater. Earth and Planetary Science Letters, 50 (1), 105-114. doi: 10.1016/0012-821X(80)90122-3

Elsworth, G., Galbraith, E., Halverson, G.P., Yang, S., 2017. Enhanced weathering and CO_2 drawdown caused by latest Eocene strengthening of the Atlantic meridional overturning circulation. Nature Geoscience, 10 (3), 213. doi: 10.1038/ngeo2888

Evans, D.A., 1998. True polar wander, a supercontinental legacy. Earth and Planetary Science Letters, 157 (1-2), 1-8. doi: 10.1016/S0012-821X(98)00031-4

Fairchild, I.J., Hambrey, M.J., 1995. Vendian basin evolution in East Greenland and NE Svalbard. Precambrian Research, 73 (1-4), 217-233. doi: 10.1016/0301-9268(94)00079-7

Falkowski, P.G., 1997. Evolution of the nitrogen cycle and its influence on the biological sequestration of CO2 in the ocean. Nature, 387 (6630), 272. doi: 10.1038/387272a0

Feng, X., Redfern, S.A., 2018. Iodate in calcite, aragonite and vaterite $CaCO_3$: Insights from first-principles calculations and implications for the I/Ca geochemical proxy. Geochimica et Cosmochimica Acta. dio: 10.1016/j.gca.2018.02.017

Gibson, T.M., Shih, P.M., Cumming, V.M., Fischer, W.W., Crockford, P.W., Hodgskiss, M.S., Wörndle, S., Creaser, R.A., Rainbird, R.H., Skulski, T.M., Halverson, G.P., 2017a. Precise age of Bangiomorpha pubescens dates the origin of eukaryotic photosynthesis. Geology, 46 (2), 135-138. doi: 10.1130/G39829.1

Gibson, T.M., Wörndle, S., Halverson, G.P., Agic, H., Lamothe, K.G., Rainbird, R.H., Skulski, T., 2017b. Composite stratigraphic section of exceptionally exposed middle Bylot Supergroup carbonate rocks along Tremblay Sound, northwestern Baffin Island, Nunavut. Summary of Activities 2017, Canada-Nunavut Geoscience Office, 81-92.

Gilleaudeau, G.J., Frei, R., Kaufman, A.J., Kah, L.C., Azmy, K., Bartley, J.K., Chernyavskiy, P., Knoll, A.H., 2016. Oxygenation of the mid-Proterozoic atmosphere: clues from chromium isotopes in carbonates. Geochemical Perspectives Letters, 2, 178-187. doi: 10.7185/geochemlet.1618

Glock, N., Liebetrau, V., Eisenhauer, A., 2014. I/Ca ratios in benthic foraminifera from the Peruvian oxygen minimum zone: analytical methodology and evaluation as proxy for redox conditions. Biogeosciences (BG), 11, 7077-7095. doi: 10.5194/bg-11-7077-2014.

Gold, T., 1955. Instability of the Earth's axis of rotation. Nature, 175 (4456), 526. doi: 10.1038/175526a0

Guilbaud, R., Poulton, S.W., Butterfield, N.J., Zhu, M., Shields-Zhou, G.A., 2015. A global transition to ferruginous conditions in the early Neoproterozoic oceans. Nature Geoscience, 8 (6), 466. doi: 10.1038/ngeo2434

Halverson, G.P., 2006. A Neoproterozoic chronology. Neoproterozoic geobiology and paleobiology (27), 231-271.

Halverson, G.P., Hoffman, P.F., Schrag, D.P., Maloof, A.C., Rice, A.H.N., 2005. Toward a Neoproterozoic composite carbon-isotope record. Geological Society of America Bulletin, 117 (9-10), 1181-1207. doi: 10.1130/B25630.1

Halverson, G.P., Kunzmann, M., Strauss, J.V., Maloof, A.C., 2018. The Tonian-Cryogenian transition in Northeastern Svalbard. Precambrian Research, 319, 79-95. doi: 10.1016/j.precamres.2017.12.010.

Halverson, G.P., Maloof, A.C., Schrag, D.P., Dudás, F.Ö., Hurtgen, M., 2007. Stratigraphy and geochemistry of a ca 800 Ma negative carbon isotope interval in northeastern Svalbard. Chemical Geology, 237 (1), 5-27. doi: 10.1016/j.chemgeo.2006.06.013

Halverson, G.P., Wade, B.P., Hurtgen, M.T., Barovich, K.M., 2010. Neoproterozoic chemostratigraphy. Precambrian Research, 182 (4), 337-350. doi: 10.1016/j.precamres.2010.04.007

Halverson, G.P., Porter, S.M., Gibson, T.M., 2018b. Dating the late Proterozoic stratigraphic record. Emerging Topiocs in Life Sciences, doi:10.1042/ETLS20170167

Hambrey, M.J., Spencer, A. M., 1987. Late Precambrian glaciation of central East Greenland. Meddelelser om Grønland Geoscience, 19.

Hardisty, D.S., Lu, Z., Bekker, A., Diamond, C.W., Gill, B.C., Jiang, G., Kah L.C., Knoll A.H., Loyd, S.J., Osburn, M.R., Planavsky, N.J., Wang, C., Zhou, X., Lyons, T.W., 2017. Perspectives on Proterozoic surface ocean redox from iodine contents in ancient and recent carbonate. Earth and Planetary Science Letters, 463, 159-170. doi: 10.1016/j.epsl.2017.01.032

Hardisty, D.S., Lu, Z., Planavsky, N.J., Bekker, A., Philippot, P., Zhou, X., Lyons, T. W., 2014. An iodine record of Paleoproterozoic surface ocean oxygenation. Geology, 42 (7), 619-622. doi: 10.1130/G35439.1

Harlan, S.S., Heaman, L., LeCheminant, A.N., Premo, W.R., 2003. Gunbarrel mafic magmatic event: A key 780 Ma time marker for Rodinia plate reconstructions. Geology, 31 (12), 1053-1056. doi: 10.1130/G19944.1

Higgins, J.A., Blättler, C.L., Lundstrom, E.A., Santiago-Ramos, D.P., Akhtar, A.A., Crüger Ahm, A-S. C., Bialik, O., Holmden, C., Bradburry, H., Murray, S.T., Swart, P.K. (2018). Mineralogy, early marine diagenesis, and the chemistry of shallow-water carbonate sediments. Geochimica et Cosmochimica Acta, 220, 512-534. doi: 10.1016/j.gca.2017.09.046

Hill, A.C., Walter, M.R., 2000. Mid-Neoproterozoic (~830–750 Ma) isotope stratigraphy of Australia and global correlation. Precambrian Research, 100 (1), 181-211. doi: 10.1016/S0301-9268(99)00074-1

Hoffman, P.F., Halverson, G.P., Domack, E.W., Maloof, A.C., Swanson-Hysell, N.L., Cox, G.M., 2012. Cryogenian glaciations on the southern tropical paleomargin of Laurentia (NE Svalbard and East Greenland), and a primary origin for the upper Russøya (Islay) carbon isotope excursion. Precambrian Research, 206, 137-158. doi: 10.1016/j.precamres.2012.02.018

Holland, H.D., 2006. The oxygenation of the atmosphere and oceans. Philosophical Transactions of the Royal Society of London B: Biological Sciences, 361 (1470), 903-915. doi: 10.1098/rstb.2006.1838

Horton, F., 2015. Did phosphorus derived from the weathering of large igneous provinces fertilize the Neoproterozoic ocean? Geochemistry, Geophysics, Geosystems, 16 (6), 1723-1738. doi: 10.1002/2015GC005792

Immenhauser, A., Della Porta, G., Kenter, J.A., Bahamonde, J.R., 2003. An alternative model for positive shifts in shallow-marine carbonate δ13C and $\delta^{18}O$. Sedimentology, 50 (5), 953-959. doi: 10.1046/j.1365-3091.2003.00590.x

Jickells, T.D., Boyd, S.S., Knap, A.H., 1988. Iodine cycling in the Sargasso Sea and the Bermuda inshore waters. Marine Chemistry, 24 (1), 61-82. doi: 10.1016/0304-4203(88)90006-0

Johnston, D.T., Poulton, S.W., Dehler, C., Porter, S., Husson, J., Canfield, D.E., Knoll, A. H., 2010. An emerging picture of Neoproterozoic ocean chemistry: Insights from the Chuar Group, Grand Canyon, USA. Earth and Planetary Science Letters, 290 (1), 64-73. doi: 10.1016/j.epsl.2009.11.059

Jones, C., Nomosatryo, S., Crowe, S.A., Bjerrum, C.J., Canfield, D.E., 2015. Iron oxides, divalent cations, silica, and the early earth phosphorus crisis. Geology, 43 (2), 135-138. doi: 10.1130/G36044.1

Kah, L.C., Lyons, T.W., Chesley, J.T., 2001. Geochemistry of a 1.2 Ga carbonate-evaporite succession, northern Baffin and Bylot Islands: implications for Mesoproterozoic marine evolution. Precambrian Research, 111 (1), 203-234. doi: 10.1016/S0301-9268(01)00161-9

Kah, L.C., Lyons, T.W., Frank, T.D., 2004. Low marine sulphate and protracted oxygenation of the Proterozoic biosphere. Nature, 431 (7010), 834-838. doi: 10.1038/nature02974

Kah, L.C., Sherman, A.G., Narbonne, G.M., Knoll, A.H., Kaufman, A.J., 1999. $\delta^{13}C$ stratigraphy of the Proterozoic Bylot Supergroup, Baffin Island, Canada: implications for regional lithostratigraphic correlations. Canadian Journal of Earth Sciences, 36 (3), 313-332. doi: 10.1139/e98-100

Katz, H.R., 1961. Late Precambrian to Cambrian stratigraphy in East Greenland. In G. O. Raasch (ed.), Geology of the Arctic 1. Toronto University Press (Toronto), 299-328.
Kaufman, A.J., Knoll, A.H., Narbonne, G.M., 1997. Isotopes, ice ages, and terminal Proterozoic earth history. Proceedings of the National Academy of Sciences, 94 (13), 6600-6605. doi: 10.1073/pnas.94.13.6600

Kennet, J.P., 1977. Cenozoic evolution of Antarctic glaciation, the circum-Antarctic Ocean, and their impact on global paleogeography. Journal of Geophysical Research, 82, 3842-3859. doi: 10.1029/JC082i027p03843

Kerisit, S.N., Smith, F.N., Saslow, S.A., Hoover, M.E., Lawter, A.R., Qafoku, N.P., 2018. Incorporation Modes of Iodate in Calcite. Environmental science & technology, 52 (10), 5902-5910. doi: 10.1021/acs.est.8b00339

Kirschvink, J.L., Ripperdan, R.L., Evans, D.A., 1997. Evidence for a large-scale reorganization of Early Cambrian continental masses by inertial interchange true polar wander. Science, 277 (5325), 541-545. doi: 10.1126/science.277.5325.541

Knoll, A.H., 1992. The early evolution of eukaryotes: a geological perspective. Science, 256 (5057), 622. doi: 10.1126/science.1585174

Knoll, A.H., 2003. The geological consequences of evolution. Geobiology, 1 (1), 3-14. doi: 10.1046/j.1472-4669.2003.00002.x

Knoll, A.H., 2014. Paleobiological perspectives on early eukaryotic evolution. Cold Spring Harbor Perspectives in Biology, 6 (1).

Knoll, A.H., Hayes, J.M., Kaufman, A.J., Swett, K., Lambert, I.B., 1986. Secular variation in carbon isotope ratios from Upper Proterozoic successions of Svalbard and East Greenland. Nature, 321, 832-838. doi: 10.1038/321832a0

Knoll, A.H., Sperling, E.A., 2014. Oxygen and animals in Earth history. Proceedings of the National Academy of Sciences, 111 (11), 3907-3908. doi: 10.1073/pnas.1401745111

Knoll, A.H., Swett, K., 1987. Micropaleontology across the Precambrian-Cambrian boundary in Spitsbergen. Journal of Paleontology, 61, 898-926. doi: 10.1017/S0022336000029292

Knoll, A.H., Swett, K., 1990. Carbonate deposition during the late Proterozoic Era: an example from Spitsbergen. American Journal of Science, 290, 104-132.

Knoll, A.H., Walker, J.C.G., 1990. The environmental context of early Metazoan evolution. Geological Society of America, 22.

Knoll, A.H., Wörndle, S., Kah, L.C., 2013. Covariance of microfossil assemblages and microbialite textures across an upper Mesoproterozoic carbonate platform. Palaios, 28 (7), 453-470. doi: 10.2110/palo.2013.p13-005r

Kump, L.R., 1991. Interpreting carbon-isotope excursions: Strangelove oceans. Geology, 19 (4), 299-302. doi: 10.1130/0091-7613(1991)019

Kump, L.R., Arthur, M. A., 1999. Interpreting carbon-isotope excursions: carbonates and organic matter. Chemical Geology, 161 (1), 181-198. doi: 10.1016/S0009-2541(99)00086-8

Kump, L.R., Arthur, M.A., Patzkowsky, M.E., Gibbs, M.T., Pinkus, D.S., Sheehan, P.M., 1999. A weathering hypothesis for glaciation at high atmospheric pCO 2 during the Late Ordovician. Palaeogeography, Palaeoclimatology, Palaeoecology, 152 (1), 173-187. doi: 10.1016/S0031-0182(99)00046-2

Kunzmann, M., Bui, T.H., Crockford, P.W., Halverson, G.P., Scott, C., Lyons, T.W., Wing, B.A., 2017a. Bacterial sulfur disproportionation constrains timing of Neoproterozoic oxygenation. Geology, 45 (3), 207-210. doi: 10.1130/G38602.1

Kunzmann, M., Gibson, T.M., Halverson, G.P., Hodgskiss, M.S.W, Bui, T.H., Carozza, D.A., Sperling, E.A., Poirier, A., Cox, G.M., Wing, B.A., 2017b. Iron isotope

biogeochemistry of Neoproterozoic marine shales. Geochimica et Cosmochimica Acta, 209, 85-105. doi: 10.1016/j.gca.2017.04.003

Kunzmann, M., Halverson, G.P., Macdonald, F.A., Hodgskiss, M.S.W., Sansjofre, P.D., Schumann, D., Rainbird, R.H., 2014. The early Neoproterozoic Chandindu Formation of the Fifteenmile Group in the Ogilvie Mountains. Yukon Exploration and Geology 2013: Yukon Geological Survey, 93-107.

Kunzmann, M., Halverson, G.P., Scott, C., Minarik, W.G., Wing, B.A., 2015. Geochemistry of Neoproterozoic black shales from Svalbard: Implications for oceanic redox conditions spanning Cryogenian glaciations. Chemical Geology, 417, 383-393. doi: 10.1016/j.chemgeo.2015.10.022

Latysheva, N., Junker, V.L., Palmer, W.J., Codd, G.A., Barker, D., 2012. The evolution of nitrogen fixation in cyanobacteria. Bioinformatics, 28 (5), 603-606. doi: 10.1093/bioinformatics/bts008

Leslie, C.D., 2009. Detrital zircon geochronology and rift related magmatism: Central Mackenzie Mountains. Northwest Territories [MS thesis]: Vancouver, University of British Columbia.

Long, D.G., Turner, E.C., 2012. Tectonic, sedimentary and metallogenic re-evaluation of basal strata in the Mesoproterozoic Bylot basins, Nunavut, Canada: Are unconformity-type uranium concentrations a realistic expectation? Precambrian Research, 214, 192-209. doi: 10.1016/j.precamres.2011.11.005

Loope, G.R., Kump, L.R., Arthur, M.A., 2013. Shallow water redox conditions from the Permian–Triassic boundary microbialite: The rare earth element and iodine geochemistry of carbonates from Turkey and South China. Chemical Geology, 351, 195-208. doi: 0.1016/j.chemgeo.2013.05.014

Li, Z.X., Evans, D.A., Halverson, G.P., 2013. Neoproterozoic glaciations in a revised global palaeogeography from the breakup of Rodinia to the assembly of Gondwanaland. Sedimentary Geology, 294, 219-232. doi: 10.1016/j.sedgeo.2013.05.016

Li, Z.X., Evans, D.A., Zhang, S., 2004. A 90° spin on Rodinia: possible causal links between the Neoproterozoic supercontinent, superplume, true polar wander and low-latitude glaciation. Earth and Planetary Science Letters, 220 (3), 409-421. doi: 10.1016/S0012-821X(04)00064-0

Lu, W., Ridgwell, A., Thomas, E., Hardisty, D.S., Luo, G., Algeo, T.J., Saltzman, M.R., Gill, B.C., Shen, Y., Ling, H-F., Edwards, C.T., Whalen, M.T., Zhou, X., Gutchess, K.M., Jin, L., Rickaby, R.E.M., Jenkyns, H.C., Lyons, T.W., Lenton, T.M., Kump, L.R., Lu, Z., 2018. Late inception of a resiliently oxygenated upper ocean. Science. doi: 10.1126/science.aar5372

Lu, W., Wörndle, S., Halverson, G.P., Zhou, X., Bekker, A., Rainbird, R.H., Hardisty, D.S., Lyons, T.W., Lu, Z., 2017. Iodine proxy evidence for increased ocean oxygenation during the Bitter Springs Anomaly. Geochemical Perspectives Letters, 5, 53-57. doi: 10.7185/geochemlet.1746

Lu, Z., Hoogakker, B.A., Hillenbrand, C.D., Zhou, X., Thomas, E., Gutchess, K.M., Lu,W., Jones, L., Rickaby, R.E., 2016. Oxygen depletion recorded in upper waters of the glacial Southern Ocean. Nature communications, 7. doi: 10.1038/ncomms11146

Lu, Z., Jenkyns, H.C., Rickaby, R.E., 2010. Iodine to calcium ratios in marine carbonate as a paleo-redox proxy during oceanic anoxic events. Geology, 38 (12), 1107-1110. doi: 10.1130/G31145.1

Luther, G.W., Campbell, T., 1991. Iodine speciation in the water column of the Black Sea. Deep Sea Research Part A. Oceanographic Research Papers, 38, S875-S882. doi: 10.1016/S0198-0149(10)80014-7

Luther, G.W., Cole, H., 1988. Iodine speciation in Chesapeake Bay waters. Marine Chemistry, 24 (3-4), 315-325. doi: 10.1016/0304-4203(88)90039-4

Lyons, T.W., Reinhard, C.T., Planavsky, N.J., 2014. The rise of oxygen in Earth's early ocean and atmosphere. Nature, 506 (7488), 307-315. doi: 10.1038/nature13068

Macdonald, F.A., Halverson, G.P., Strauss, J.V., Smith, E.F., Cox, G., Sperling, E.A., Roots, C.F., 2012. Early Neoproterozoic Basin Formation in Yukon, Canada: Implications for the make-up and break-up of Rodinia. Geoscience Canada, 39 (2).

Macdonald, F.A., Smith, E.F., Strauss, J.V., Cox, G.M., Halverson, G.P., Roots, C.F., 2010. Neoproterozoic and early Paleozoic correlations in the western Ogilvie Mountains, Yukon. Yukon Exploration and Geology, 161-182.

Macdonald, F.A., Strauss, J.V., Sperling, E.A., Halverson, G.P., Narbonne, G.M., Johnston, D.T., Kunzmann, M., Schrag, D.P., Higgins, J.A., 2013. The stratigraphic relationship between the Shuram carbon isotope excursion, the oxygenation of Neoproterozoic oceans, and the first appearance of the Ediacara biota and bilaterian trace fossils in northwestern Canada. Chemical Geology, 362, 250-272. doi: 10.1016/j.chemgeo.2013.05032

Maloof, A.C., Halverson, G.P., Kirschvink, J.L., Schrag, D.P., Weiss, B.P., Hoffman, P.F., 2006. Combined paleomagnetic, isotopic, and stratigraphic evidence for true polar wander from the Neoproterozoic Akademikerbreen Group, Svalbard, Norway. Geological Society of America Bulletin, 118 (9-10), 1099-1124. doi: 10.1130/B25892.1

Matsuyama, I., Mitrovica, J.X., Manga, M., Perron, J.T., Richards, M.A., 2006. Rotational stability of dynamic planets with elastic lithospheres. Journal of Geophysical Research: Planets, 111 (E2). doi: 10.1029/2005JE002447

Milne, G.A., Mitrovica, J.X., 1996. Postglacial sea-level change on a rotating Earth: first results from a gravitationally self-consistent sea-level equation. Geophysical Journal International, 126 (3), F13-F20. doi: 10.1111/j.1365-246X.1996.tb04691.x

Muttoni, G., Dallanave, E., Channell, J.E.T., 2013. The drift history of Adria and Africa from 280 Ma to Present, Jurassic true polar wander, and zonal climate control

on Tethyan sedimentary facies. Palaeogeography,Palaeoclimatology, Palaeoecology, 386, 415-435. doi: 10.1016/j.palaeo.2013.06.011

Mitrovica, J.X., Milne, G.A., 1998. Glaciation-induced perturbations in the Earth's rotation: a new appraisal. Journal of Geophysical Research: Solid Earth, 103 (B1), 985-1005. doi: 10.1029/97JB02121

Mound, J.E., Mitrovica, J.X., Evans, D.A., Kirschvink, J.L., 1999. A sea-level test for inertial interchange true polar wander events. Geophysical Journal International, 136 (3), F5-F10. doi: 10.1046/j.1365-246x.1999.00791.x

Och, L.M., Shields-Zhou, G.A., 2012. The Neoproterozoic oxygenation event: environmental perturbations and biogeochemical cycling. Earth-Science Reviews, 110 (1), 26-57. doi: 10.1016/j.earscirev.2011.09.004

Petersen, G.W., Chesters, G., 1966. Quantitative determination of calcite and dolomite in pure carbonates and limestones. European Journal of Soil Science, 17 (2), 317-327. doi: 10.1111/j.1365-2389.1966.tb01476.x

Planavsky, N. J., Reinhard, C.T., Wang, X., Thomson, D., McGoldrick, P., Rainbird, R.H., Johnson, T., Fisher, W.W., Lyons, T.W., 2014. Low Mid-Proterozoic atmospheric oxygen levels and the delayed rise of animals. Science, 346 (6209), 635-638. doi: 10.1126/science.1258410

Planavsky, N.J., Rouxel, O.J., Bekker, A., Lalonde, S.V., Konhauser, K.O., Reinhard, C.T., Lyons, T.W., 2010. The evolution of the marine phosphate reservoir. Nature, 467 (7319), 1088-1090. doi: 10.1038/nature09485

Podder, J., Lin, J., Sun, W., Botis, S.M., Tse, J., Chen, N., Hu, Y., Li, D., Seaman, J., Pan, Y., 2017. Iodate in calcite and vaterite: Insights from synchrotron X-ray absorption spectroscopy and first-principles calculations. Geochimica et Cosmochimica Acta, 198, 218-228. doi: 10.1016/j.gca.2016.11.032

Poulton, S.W., Fralick, P.W., Canfield, D.E., 2010. Spatial variability in oceanic redox structure 1.8 billion years ago. Nature Geoscience, 3 (7), 486-490. doi: 10.1038/ngeo889

Prince, J.K.G., Rainbird, R.H., Wing, B.A., 2019. Evaporite deposition in the mid-Neoproterozoic as a driver for changes in seawater chemistry and the biogeochemical cycle of sulfur. Geology, 47, 375–379. doi: 10.1130/G45464.1

Rainbird, R.H., Jefferson, C.W., Young, G.M., 1996. The early Neoproterozoic sedimentary Succession B of northwestern Laurentia: Correlations and paleogeographic significance. Geological Society of America Bulletin, 108 (4), 454-470. doi: 10.1130/0016-7606(1996)108

Reinhard, C.T., Planavsky, N.J., Gill, B.C., Ozaki, K., Robbins, L.J., Lyons, T.W., Fisher, W.W., Chunjiang. W., Cole. D.B., Konhauser, K.O., 2017. Evolution of the global phosphorus cycle. Nature, 541 (7637), 386-389. doi: 10.1038/nature20772

Reinhard, C.T., Planavsky, N.J., Olson, S.L., Lyons, T.W., Erwin, D.H., 2016. Earth's oxygen cycle and the evolution of animal life. Proceedings of the National Academy of Sciences, 113 (32), 8933-8938. doi: 10.1073/pnas.1521544113

Reinhard, C.T., Planavsky, N.J., Robbins, L.J., Partin, C.A., Gill, B.C., Lalonde, S.V., Bekker, A., Konhauser, K.O., Lyons, T.W., 2013. Proterozoic ocean redox and biogeochemical stasis. Proceedings of the National Academy of Sciences, 110 (14), 5357-5362. doi: 10.1073/pnas.1208622110

Riedman, L.A., Sadler, P.M., 2017. Global species richness record and biostratigraphic potential of early to middle Neoproterozoic eukaryote fossils. Precambrian Research. doi: 10.1016/j.precamres.2017.10.008

Robson, R.L., Eady, R.R., Richardson, T.H., Miller, R.W., Hawkins, M., Postgate, J.R., 1986. The alternative nitrogenase of Azotobacter chroococcum is a vanadium enzyme. Nature, 322 (6077), 388-390. doi: 10.1038/3222388a0

Shields, G.A., Mills, B.J., 2017. Tectonic controls on the long-term carbon isotope mass balance. *Proceedings of the National Academy of Sciences*, 201614506. doi: 10.1073/pnas.1614506114

Sperling, E.A., Halverson, G.P., Knoll, A.H., Macdonald, F.A., Johnston, D.T., 2013. A basin redox transect at the dawn of animal life. Earth and Planetary Science Letters, 371, 143-155. doi: 10.1016/j.epsl.2013.04.003

Sperling, E.A., Rooney, A.D., Hays, L., Sergeev, V.N., Vorob'eva, N.G., Sergeeva, N.D., Selby, D., Johnston, D.T., Knoll, A.H., 2014. Redox heterogeneity of subsurface waters in the Mesoproterozoic ocean. Geobiology, 12 (5), 373-386. doi: 10.1111/gbi.12091

Sperling, E.A., Wolock, C.J., Morgan, A.S., Gill, B.C., Kunzmann, M., Halverson, G.P., Macdonald, F.A., Knoll, A.H., Johnston, D.T., 2015. Statistical analysis of iron geochemical data suggests limited late Proterozoic oxygenation. Nature, 523 (7561), 451-454. doi: 10.1038/nature14589

Steinberger, B., O'Connell, R.J., 1997. Changes of the Earth's rotation axis owing to advection of mantle density heterogeneities. Nature, 387, 169-173. doi: 10.1038/387169a0

Stolper, D.A., Keller, C.B., 2018. A record of deep-ocean dissolved O_2 from the oxidation state of iron in submarine basalts. Nature, 553, 323-327. doi: 10.1038/nature25009

Sundby, B., 2006. Transient state diagenesis in continental margin muds. *Marine chemistry*. 102 (1-2), 2-12. doi: 10.1016/j.marchem.2005.09.016

Swanson-Hysell, N.L., Maloof, A.C., Condon, D.J., Jenkin, G.R., Alene, M., Tremblay, M.M., Tesema, T., Rooney, A.D., Haileab, B., 2015. Stratigraphy and geochronology of the Tambien Group, Ethiopia: evidence for globally synchronous

carbon isotope change in the Neoproterozoic. Geology, 43 (4), 323-326. doi: 10.1130/G36347.1

Swanson-Hysell, N.L., Maloof, A.C., Kirschvink, J.L., Evans, D.A., Halverson, G.P., Hurtgen, M.T., 2012. Constraints on Neoproterozoic paleogeography and Paleozoic orogenesis from paleomagnetic records of the Bitter Springs Formation, Amadeus Basin, central Australia. American Journal of Science, 312 (8), 817-884. doi: 0.2475/08.2012.01

Swanson-Hysell, N.L., Rose, C.V., Calmet, C.C., Halverson, G.P., Hurtgen, M.T., Maloof, A.C., 2010. Cryogenian glaciation and the onset of carbon-isotope decoupling. Science, 328 (5978), 608-611. doi: 10.1126/science.1184508

Swart, P.K., 2008. Global synchronous changes in the carbon isotopic composition of carbonate sediments unrelated to changes in the global carbon cycle. Proceedings of the National Academy of Sciences, 105 (37), 13741-13745. doi: 10.1073/pnas.0802841105

Tagami, K., Uchida, S., 2005. Sample storage conditions and holding times for the determination of total iodine in natural water samples by ICP-MS. Atomic spectroscopy-norwalk connecticut, 26 (6), 209-214.

Thomson, D., Rainbird, R.H., Planavsky, N., Lyons, T.W., Bekker, A., 2015. Chemostratigraphy of the Shaler Supergroup, Victoria Island, NW Canada: A record of ocean composition prior to the Cryogenian glaciations. Precambrian Research, 263, 232-245. doi: 10.1026/j.precamres.2015.02.007

Thorkelson, D.J., Abbott, J.G., Mortensen, J.K., Creaser, R.A., Villeneuve, M.E., McNicoll, V.J., Layer, P.W., 2005. Early and middle Proterozoic evolution of Yukon, Canada. Canadian Journal of Earth Sciences, 42 (6), 1045-1071. doi: 10.1139/e04-075

Thorkelson, D.J., Laughton, J.R., Hunt, J.A., Baker, T., 2002. Geology and mineral occurrences of the Quartet Lakes map area (NTS 106E/1), Wernecke and Mackenzie mountains, Yukon. Yukon exploration and geology, 223-239.

Tsunogai, S., 1971. Iodine in the deep water of the ocean. In Deep Sea Research and Oceanographic Abstracts, 18 (9), 913-919. doi: 10.1016/0011-7471(71)90065-9

Tsunogai, S., Henmi, T., 1971. Iodine in the surface water of the ocean. Journal of the Oceanographical Society of Japan, 27 (2), 67-72. doi: 10.1007/BF021109332

Tsunogai, S., Sase, T., 1969. Formation of iodide-iodine in the ocean. Deep Sea Research and Oceanographic Abstracts, 16 (5), 489-496. doi: 10.1016/0011-7471(69)90037-0

Truesdale, V.W., Bale, A.J., Woodward, E.M.S., 2000. The meridional distribution of dissolved iodine in near-surface waters of the Atlantic Ocean. Progress in Oceanography, 45 (3-4), 387-400. doi: 10.1016/S0079-6611(00)00009-4

Truesdale, V.W., Bailey, G.W., 2000. Dissolved iodate and total iodine during an extreme hypoxic event in the Southern Benguela system. Estuarine, Coastal and Shelf Science, 50 (6), 751-760. doi: 10.1006/ecss.2000.0609

Turner, E.C., Bekker, A., 2016. Thick sulfate evaporite accumulations marking a mid-Neoproterozoic oxygenation event (Ten Stone Formation, Northwest Territories, Canada). Bulletin, 128 (1-2), 203-222. doi: 10.1130/B31268.1

Turner, E.C., Long, D.G., 2008. Basin architecture and syndepositional fault activity during deposition of the Neoproterozoic Mackenzie Mountains Supergroup, Northwest Territories, Canada Northwest Territories Geoscience Office Contribution 0040. Canadian Journal of Earth Sciences, 45 (10), 1159-1184. doi: 10.1139/E08-062

Turner, E.C., Long, D.G.F., 2012. Formal definition of the Neoproterozoic Mackenzie Mountains Supergroup (NWT), and formal stratigraphic nomenclature for its carbonate and evaporite formations. Geological Survey of Canada Open File, 7112, 57.

White, A.E., 2009. New insights into bacterial acquisition of phosphorus in the surface ocean. Proceedings of the National Academy of Sciences, 106 (50), 21013-21014. doi: 10.1073/pnas.0912475107

White, A.E., Spitz, Y.H., Karl, D.M., Letelier, R.M., 2006. Flexible elemental stoichiometry in Trichodesmium spp. and its ecological implications. Limnology and Oceanography, 51 (4), 1777-1790. doi: 10.4319/lo.2006.51.4.1777

Williams, R.J.P., Da Silva, J.F., 2002. The involvement of molybdenum in life. Biochemical and biophysical research communications, 292 (2), 293-299. doi: 10.1006/bbrc.2002.6518

Wong, G.T.F., Brewer, P.G., 1974. Determination and distribution of iodate in South-Atlantic waters. Journal of Marine Research, 32 (1), 25-36.

Wong, G.T., Brewer, P.G., 1976. The determination of iodide in sea water by neutron activation analysis. Analytica chimica acta, 81 (1), 81-90. doi: 10.1016/S0003-2670(00)89461-1

Yang, S., Galbraith, E., Palter, J., 2013. Coupled climate impacts of the Drake Passage and the Panama Seaway. Climate Dynamics, 43, 37-52.

Zegeye, A., Bonneville, S., Benning, L.G., Sturm, A., Fowle, D.A., Jones, C., Canfield. D.E., Ruby. C., MacLean. L.C., Nomosatryo. S., Crowe. S.A. Poulton. S.W., 2012. Green rust formation controls nutrient availability in a ferruginous water column. Geology, 40 (7), 599-602. doi: 10.1130/G32959.1

Zhang, X., Sigman, D.M., Morel, F.M., Kraepiel, A.M., 2014. Nitrogen isotope fractionation by alternative nitrogenases and past ocean anoxia. Proceedings of the National Academy of Sciences, 111 (13), 4782-4787. doi: 10.1073/pnas.1402976111

Zhou, X., Jenkyns, H.C., Owens, J.D., Junium, C.K., Zheng, X.Y., Sageman, B.B., Hardisty, D.S., Lyons, T.W., Ridgwell, A., Lu, Z., 2015. Upper ocean oxygenation

dynamics from I/Ca ratios during the Cenomanian-Turonian OAE 2. Paleoceanography, 30 (5), 510-526. doi: 10.1002/2014PA002741

Zhou, X., Thomas, E., Rickaby, R.E., Winguth, A.M., Lu, Z., 2014. I/Ca evidence for upper ocean deoxygenation during the PETM. Paleoceanography, 29 (10), 964-975. doi: 10.1002/2014PA002702

Figures

Figure 1 – Map and generalized stratigraphy of the studied area in northeastern Svalbard, Norway. a) Geological map of the glaciated Caledonian fold-and-trust belt on Nordaustlanded (*Norda.*) and Spitsbergen (*Spitsb.*) islands (modified from Hoffman et al., 2012 and Kunzmann et al., 2015), ESZ= Eolusletta Shear Zone, LFZ= Lomfjorden Fault Zone. b) Generalized lithostratigraphy (modified from Halverson et al., 2007 and Kunzmann et al., 2015). Estimated ages for the Akademikerbreen from Halverson et al. (2018b).

Figure 2 – A composite stratigraphic section through the Akademikerbreen Group in Svalbard (Halverson et al., 2018), highlighting the Bitter Springs anomaly. Vet. Gp.= Veteranen Group. The smoothed carbon isotope curve on the left is a LOWESS fit of all available $\delta^{13}C_{carb}$ data (Halverson et al., 2018b), and the data on the middle column are from the same sample sets analyzed for I/[Ca+Mg] in the right column. Arrows marking the positive excursions in the I/[Ca+Mg] record.

Figure 3 – Geological map of the study area in eastern Greenland (modified from Hoffman et al., 2012) being a part of East Greenland- East Svalbard basin (EGES).

Figure 4 – Stratigraphic log of the middle Brogetdal Formation (Ymer Ø Group) spanning the Bitter Springs Anomaly on Ymer Ø, East Greenland, with accompanying $\delta^{13}C_{carb}$ and I/[Ca+Mg] data. Note that the BSA is uncharacteristically thin in this section which could reflect either condensation of the section (in lower Bed-group 10) or missing section on the sequence boundary between Bed-groups 9 and 10. Arrow marking the positive excursion in the I/[Ca+Mg] record.

Figure 5 – Map and generalized stratigraphy of the study area in northwest Canada. a) Distribution of Proterozoic strata in the inliers in Yukon and northwest Territoires (NWT), Canada (modified from Macdonald et al., 2010 and Kunzmann et al., 2014). b) Generalized lithostratigraphy of Mackenzie Mountains (modified from Macdonald et al., 2012).

Figure 6 – Detailed Neoproterozoic stratigraphy of a measured section in Mackenzie Mountains, spanning the Bitter Springs anomaly. Snail S. Fm.= Snail Spring Formation. Carbon stable isotope record ($\delta^{13}C_{carb}$) highlighting the negative excursion characteristic of the Bitter Springs anomaly. Measurement of the ratio I/[Ca+Mg] on carbonate samples spanning the Bitter Springs anomaly.

Figure 7 – Cross-plots of I/[Ca+Mg] vs. $\delta^{13}C$ measured in carbonate samples from Akademikerbreen Group on Svalbard, Mackenzie Mountains Supergroup (MMSG) in NWT, and Ymer Ø Group on Greenland.

Figure 8 – Measurements of carbonate major elements on samples from Akademikerbreen Group on Svalbard, Mackenzie Mountains Supergroup (MMSG) in NWT, and Ymer Ø Group on Greenland. a) I/[Ca+Mg] vs. Mg/Ca exhibits no specific trend between calcite (Mg/Ca < 0.2) and dolomite (Mg/Ca > 0.6), the dolomitization does not impact the redox-proxy values; b) I/[Ca+Mg] vs. Mn/Sr displays little alteration (Mn/Sr > 2) for mostly all MMSG; c) I/[Ca+Mg] vs. Sr and d) I/[Ca+Mg] vs. Fe show low Sr and Fe concentrations associated with high I/[Ca+Mg] ratios; e) I/[Ca+Mg] vs. $\delta^{18}O$ and f) Mg/Ca vs. $\delta^{18}O$ present $\delta^{18}O$ values from MMSG with an offset (6‰) between calcite and dolomite suggesting a late stage dolomitization for these samples only.

Figure 9 – Sketches illustrating the effects of changing oceanic redox conditions along carbonate platform transect, during Bitter Springs Anomaly (BSA) stages, on the reservoirs of iodate (IO_3^-), iodide (I^-), sulfate (SO_4^{2-}), iron (Fe) and molybdenum (Mo). 1/ Pre- and post-BSA oceans present similar conditions with relatively well oxygenated surface ocean overlying deep ferruginous ocean (Fe^{2+}-enriched and anoxic) with phosphorus (P) as a biolimiting nutrient (Anbar and Knoll, 2002). This redox stratified ocean is characteristic of the Neoproterozoic Era. 2/ and 3/ The syn-BSA ocean despites bottom euxinia with nitrogen (N) as biolimiting nutrient (Anbar and Knoll, 2002). A change in the nutrient regime at the onset of BSA can lower primary production leading to low $\delta^{13}C_{carb}$ values as well as intense remineralization of organic matter; 2/ The onset of BSA (early stage) is marked by the growth of the SO_4^{2-} reservoir and the expansion of bottom euxinia with the growth of deep I^- pool. The oxycline is gradually shallowing; 3/ In the last stage, a shallower oxycline combined with a global ocean circulation reorganization at the end of BSA lead to a mixing between euxinic deep water and oxic surface water. I^- is shuffle in oxic water and oxidized to IO_3^- leading to increase of I/[Ca+Mg] values in shallow marine carbonate.

Highlights:

1. New stratigraphic and chemostratigraphic data spanning the Bitter Springs $\delta^{13}C$ anomaly
2. Application of the I/[Ca+Mg] proxy to Tonian carbonates and purported oxygenation
3. New conceptual model for the Bitter Springs anomaly based on a multi-proxy approach
4. Discerning the effects of post-depositional processes on I/[Ca+Mg] signatures

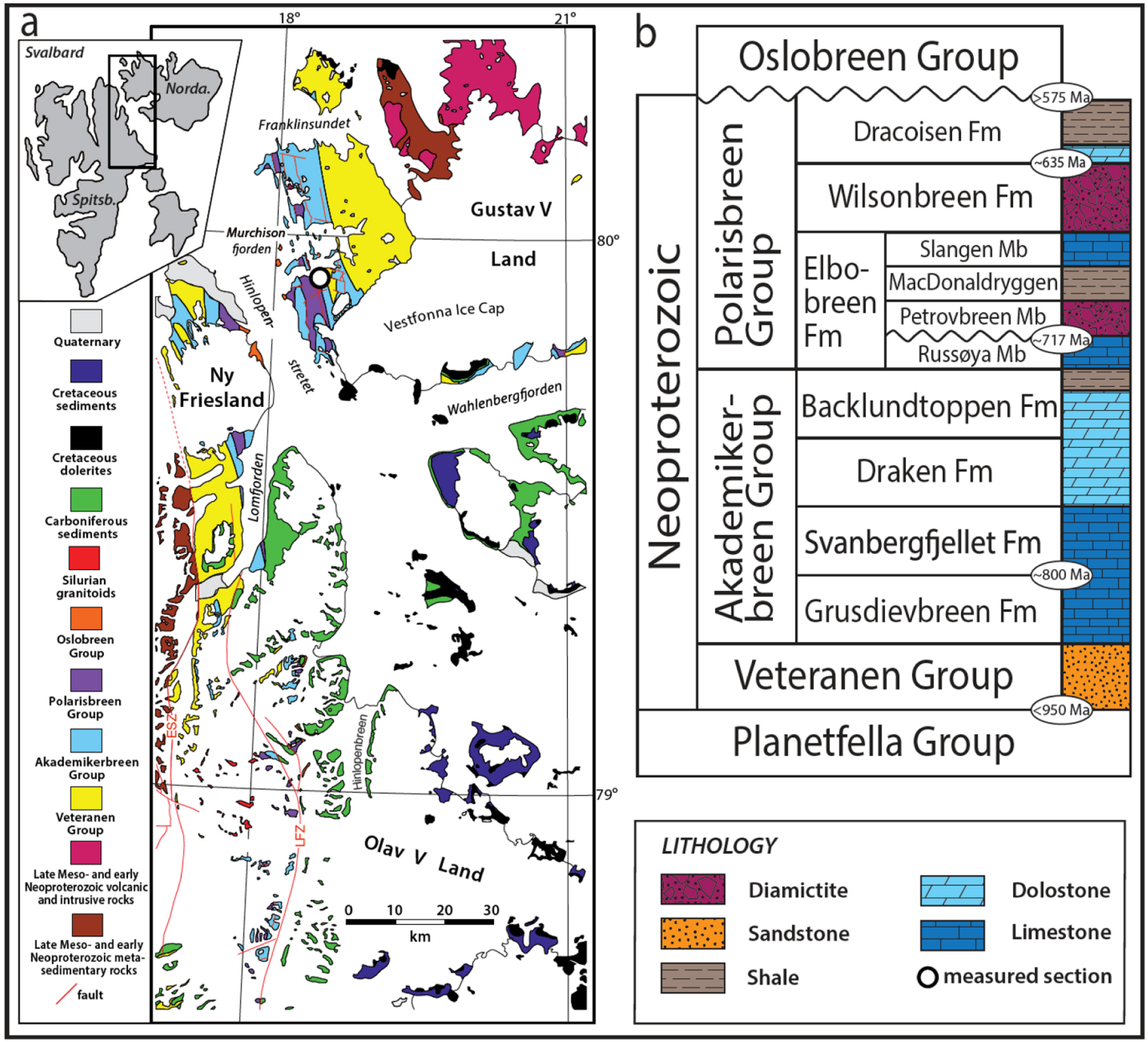
a
18°
21°
Svalbard
Norda.
Spitsb.
Franklinsundet
Gustav V
Land
Murchison fjorden
80°
Hinlopen strætet
Vestfonna Ice Cap
Ny Friesland
Wahlenbergfjorden
Lomfjorden
ESZ
LFZ
Hinlopenbreen
79°
Olav V Land
0 10 20 30
km
Quaternary
Cretaceous sediments
Cretaceous dolerites
Carboniferous sediments
Silurian granitoids
Oslobreen Group
Polarisbreen Group
Akademikerbreen Group
Veteranen Group
Late Meso- and early Neoproterozoic volcanic and intrusive rocks
Late Meso- and early Neoproterozoic meta-sedimentary rocks
fault
b
Oslobreen Group
~575 Ma
Neoproterozoic
Polarisbreen Group
Dracoisen Fm
~635 Ma
Wilsonbreen Fm
Elbo-breen Fm
Slangen Mb
MacDonaldryggen
Petrovbreen Mb
~717 Ma
Russøya Mb
Akademiker-breen Group
Backlundtoppen Fm
Draken Fm
Svanbergfjellet Fm
~800 Ma
Grusdievbreen Fm
Veteranen Group
~950 Ma
Planetfella Group
LITHOLOGY
Diamictite
Sandstone
Shale
Dolostone
Limestone
measured section

Figure 1

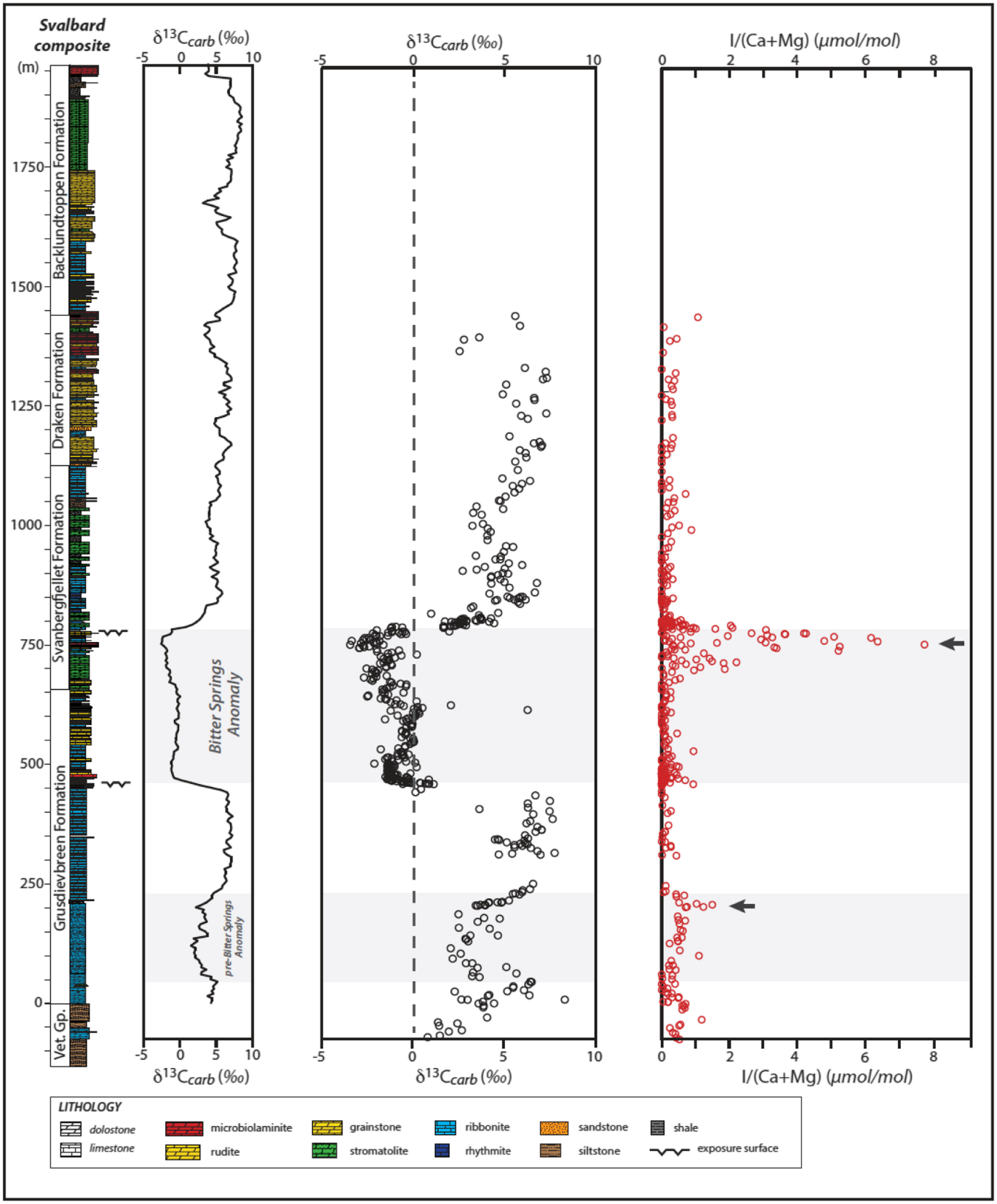
Svalbard composite
(m)
Backlundtoppen Formation
Draken Formation
Svanbergfjellet Formation
Grusdievbreen Formation
Vet. Gp.
1750
1500
1250
1000
750
500
250
0
δ13Ccarb (‰)
-5
0
5
10
Bitter Springs Anomaly
pre-Bitter Springs Anomaly
I/(Ca+Mg) (μmol/mol)
0
2
4
6
8
LITHOLOGY
dolostone
limestone
microbiolaminite
rudite
grainstone
stromatolite
ribbonite
rhythmite
sandstone
siltstone
shale
exposure surface

Figure 2

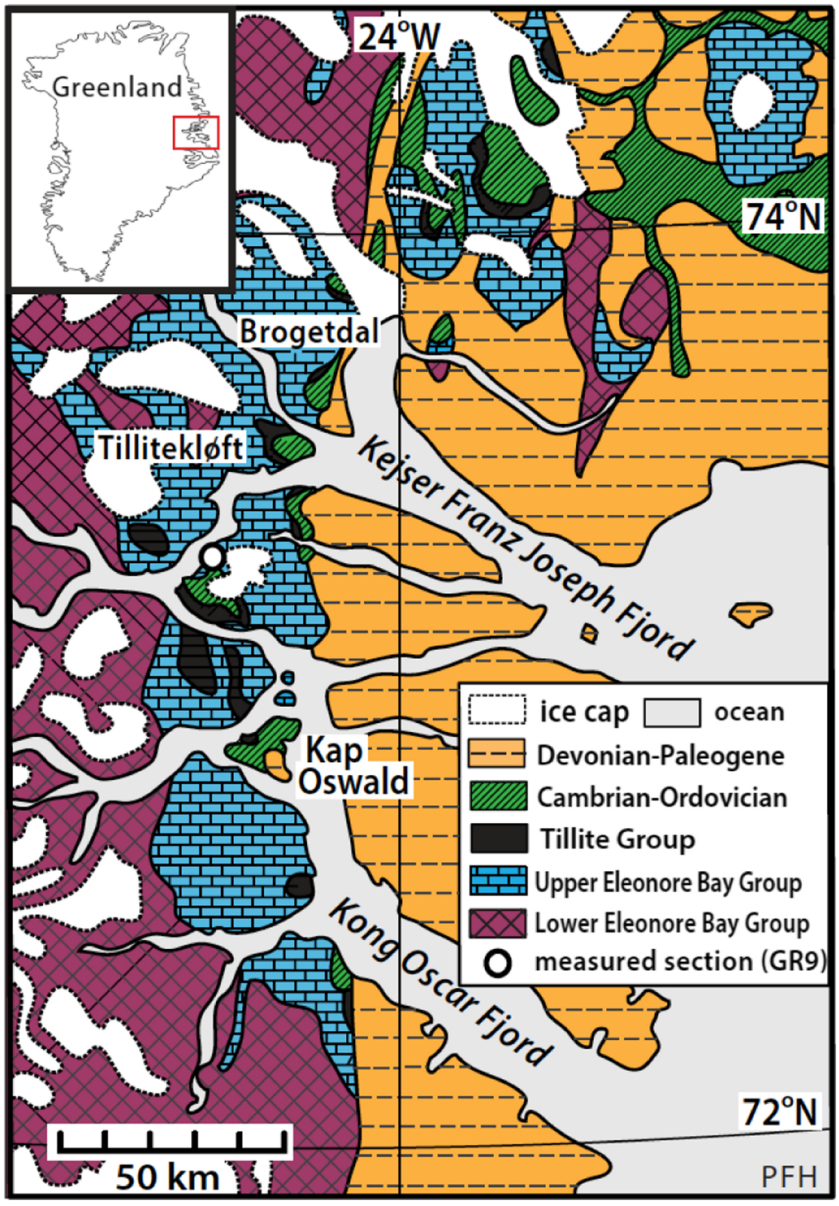
Greenland
24°W
74°N
Brogetdal
Tillitekløft
Kejser Franz Joseph Fjord
Kap Oswald
Kong Oscar Fjord
72°N
50 km
PFH
ice cap
ocean
Devonian-Paleogene
Cambrian-Ordovician
Tillite Group
Upper Eleonore Bay Group
Lower Eleonore Bay Group
measured section (GR9)

Figure 3

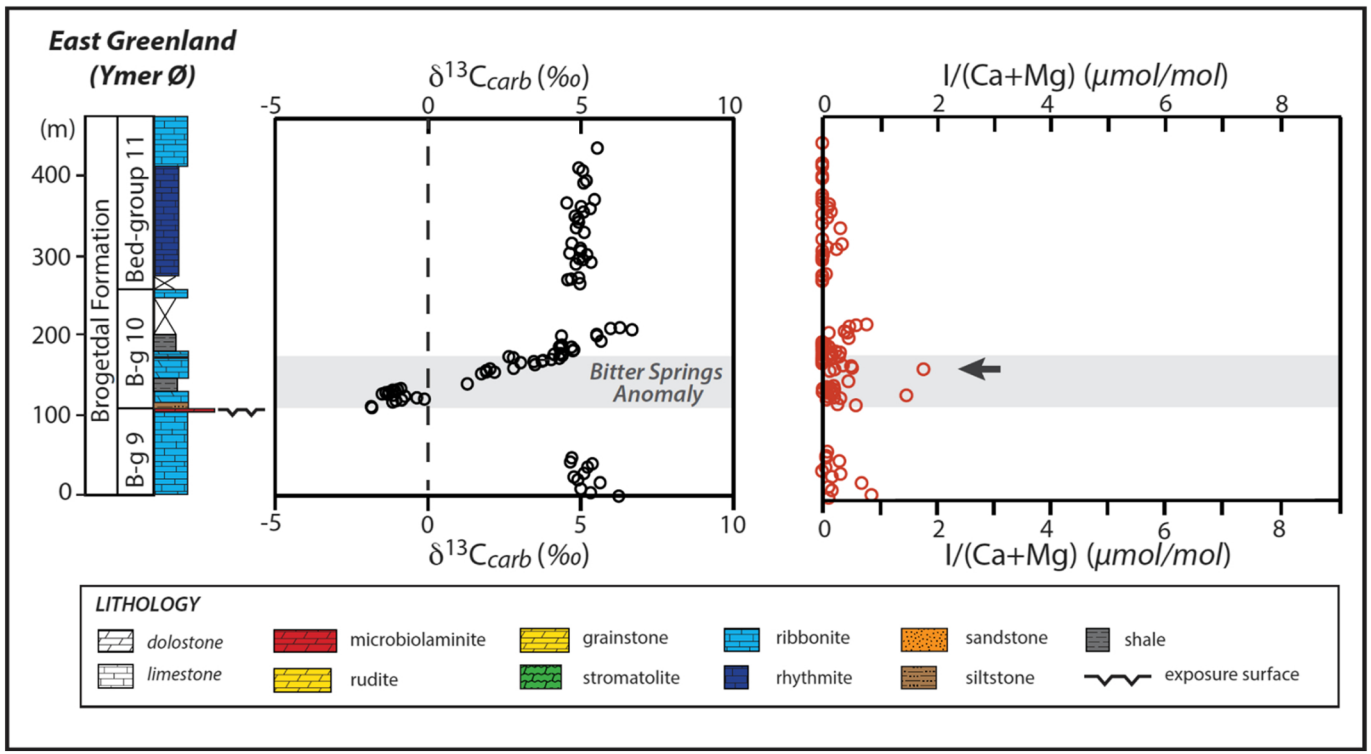
East Greenland
(Ymer Ø)
(m)
400
300
200
100
0
Brogetdal Formation
Bed-group 11
B-g 10
B-g 9
δ13Ccarb (‰)
-5
0
5
10
Bitter Springs
Anomaly
I/(Ca+Mg) (μmol/mol)
0
2
4
6
8
LITHOLOGY
dolostone
limestone
microbiolaminite
rudite
grainstone
stromatolite
ribbonite
rhythmite
sandstone
siltstone
shale
exposure surface

Figure 4

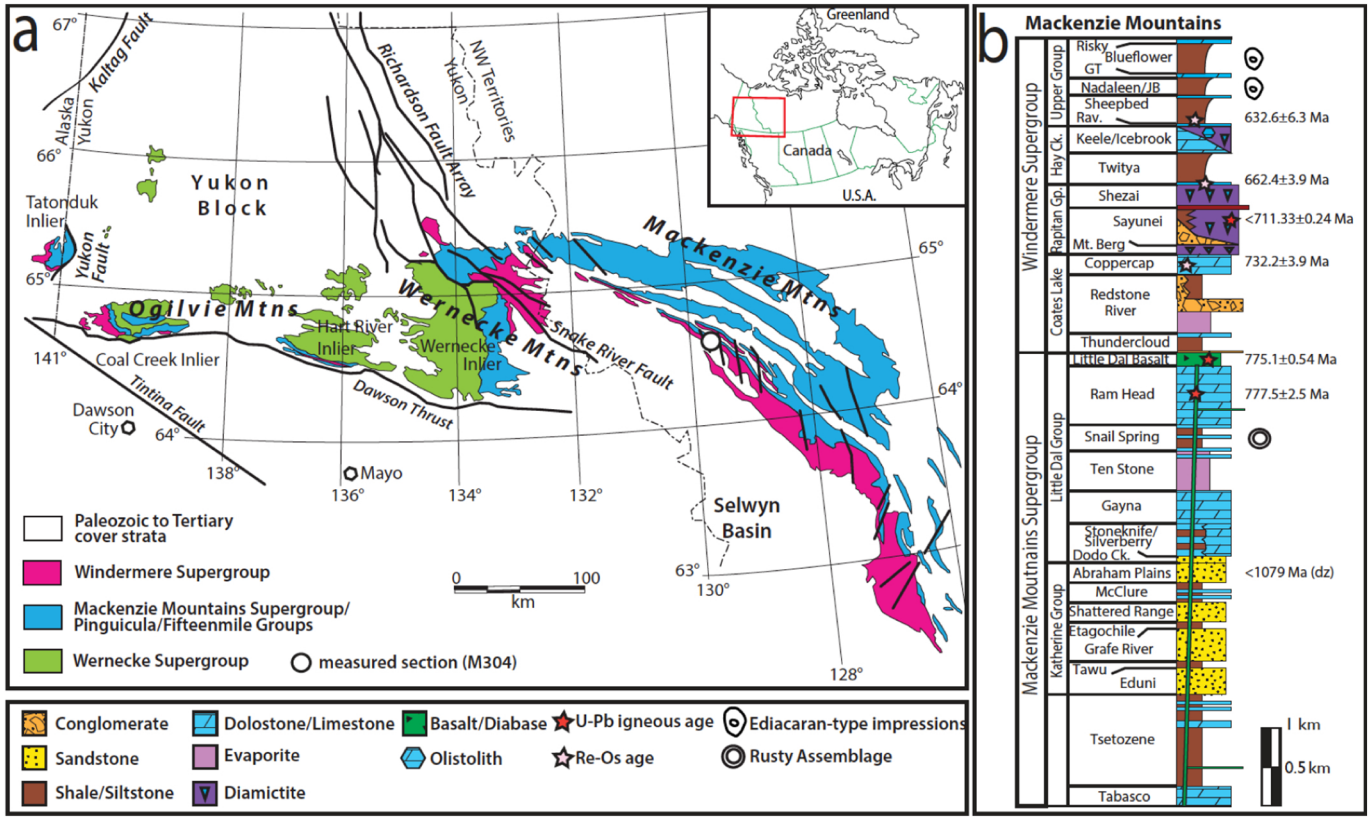
a
67°
66°
65°
64°
63°
141°
138°
136°
134°
132°
130°
128°
Alaska
Yukon
Kaltag Fault
Richardson Fault/Array
NW Territories
Yukon
Yukon Block
Tatonduk Inlier
Yukon Fault
Ogilvie Mtns
Hart River Inlier
Wernecke Inlier
Wernecke Mtns
Mackenzie Mtns
Snake River Fault
Coal Creek Inlier
Tintina Fault
Dawson Thrust
Dawson City
Mayo
Selwyn Basin
0
100
km
Greenland
Canada
U.S.A.
Paleozoic to Tertiary cover strata
Windermere Supergroup
Mackenzie Mountains Supergroup/ Pinguicula/Fifteenmile Groups
Wernecke Supergroup
measured section (M304)
Conglomerate
Sandstone
Shale/Siltstone
Dolostone/Limestone
Evaporite
Diamictite
Basalt/Diabase
Olistolith
U-Pb igneous age
Re-Os age
Ediacaran-type impressions
Rusty Assemblage
b
Mackenzie Mountains
Windermere Supergroup
Mackenzie Moutnains Supergroup
Upper Group
Hay Ck.
Rapitan Gp.
Coates Lake
Little Dal Group
Katherine Group
Risky
Blueflower
GT
Nadaleen/JB
Sheepbed
Rav.
632.6±6.3 Ma
Keele/Icebrook
Twitya
662.4±3.9 Ma
Shezai
Sayunei
<711.33±0.24 Ma
Mt. Berg
Coppercap
732.2±3.9 Ma
Redstone River
Thundercloud
Little Dal Basalt
775.1±0.54 Ma
Ram Head
777.5±2.5 Ma
Snail Spring
Ten Stone
Gayna
Stoneknife/ Silverberry
Dodo Ck.
Abraham Plains
<1079 Ma (dz)
McClure
Shattered Range
Etagochile
Grafe River
Tawu
Eduni
Tsetozene
Tabasco
1 km
0.5 km

Figure 5

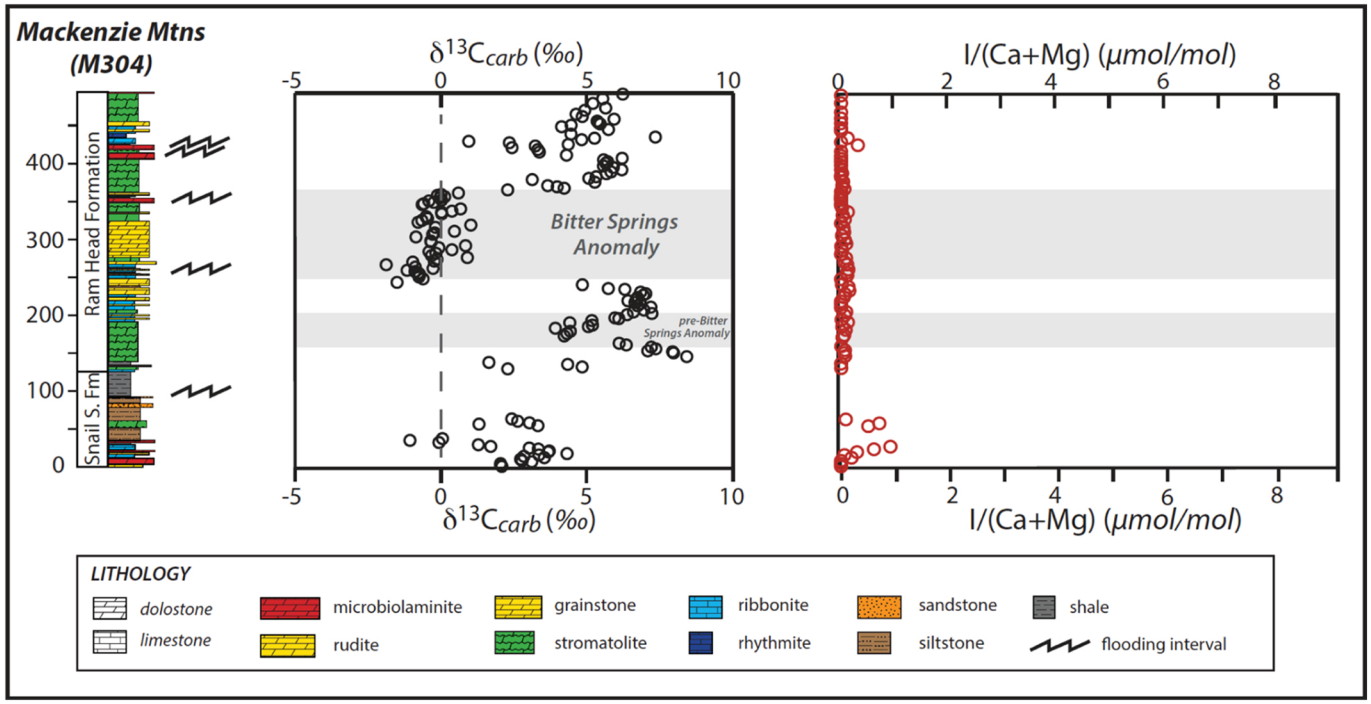
Mackenzie Mtns
(M304)
Ram Head Formation
Snail S. Fm
0
100
200
300
400
δ13Ccarb (‰)
-5
0
5
10
Bitter Springs
Anomaly
pre-Bitter
Springs Anomaly
I/(Ca+Mg) (μmol/mol)
0
2
4
6
8
LITHOLOGY
dolostone
limestone
microbiolaminite
rudite
grainstone
stromatolite
ribbonite
rhythmite
sandstone
siltstone
shale
flooding interval

Figure 6

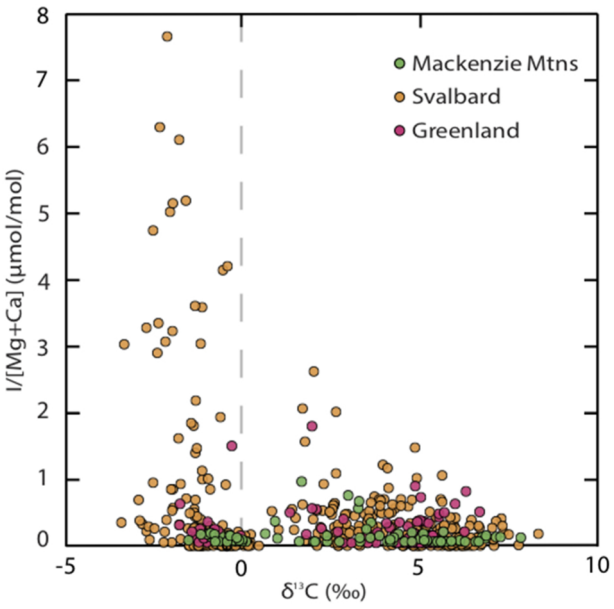
Mackenzie Mtns
Svalbard
Greenland
I/[Mg+Ca] (µmol/mol)
δ13C (‰)
8
7
6
5
4
3
2
1
0
-5
0
5
10

Figure 7

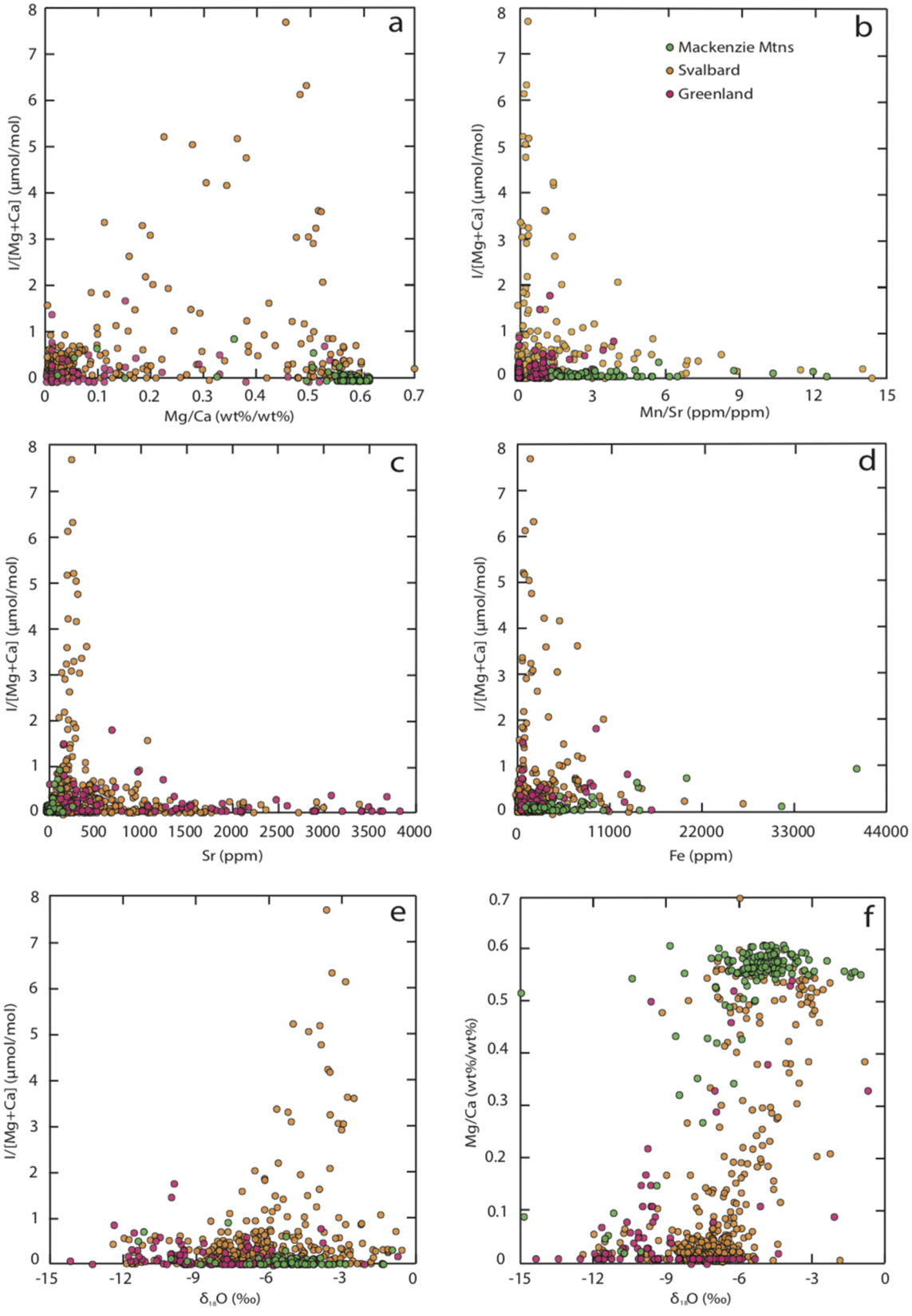
a
b
c
d
e
f
Mackenzie Mtns
Svalbard
Greenland
I/[Mg+Ca] (µmol/mol)
Mg/Ca (wt%/wt%)
Mn/Sr (ppm/ppm)
Sr (ppm)
Fe (ppm)
δ18O (‰)

Figure 8

1/ Pre-BSA and post-BSA oceans

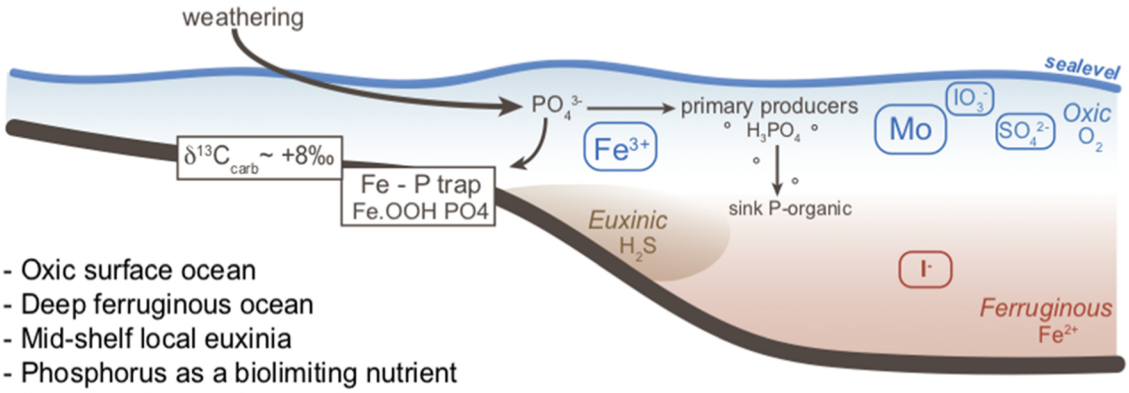

- Oxic surface ocean
- Deep ferruginous ocean
- Mid-shelf local euxinia
- Phosphorus as a biolimiting nutrient
- Growth of iron and molybdenum reservoirs

2/ Syn-BSA ocean: early stage

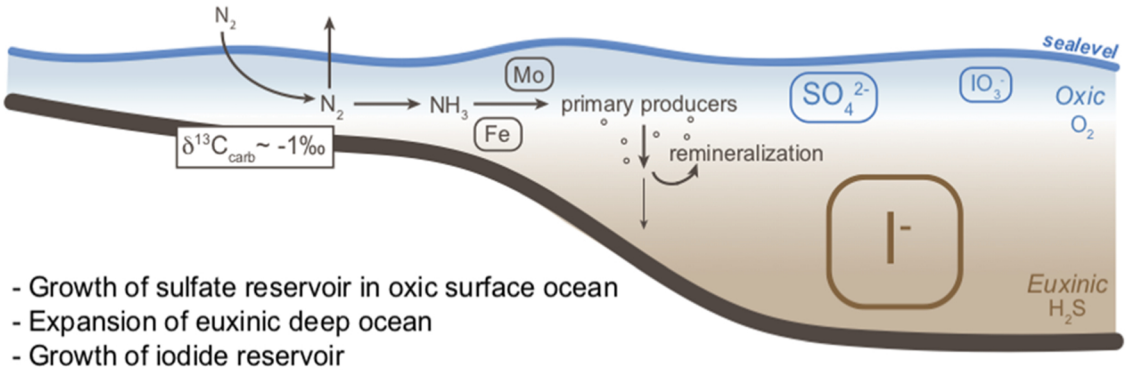

- Growth of sulfate reservoir in oxic surface ocean
- Expansion of euxinic deep ocean
- Growth of iodide reservoir
- Nitrogen as a biolimiting nutrient
- Depletion of iron and molybdenum reservoirs
- Intense remineralization of organic matter

3/ Syn-BSA ocean: last stage

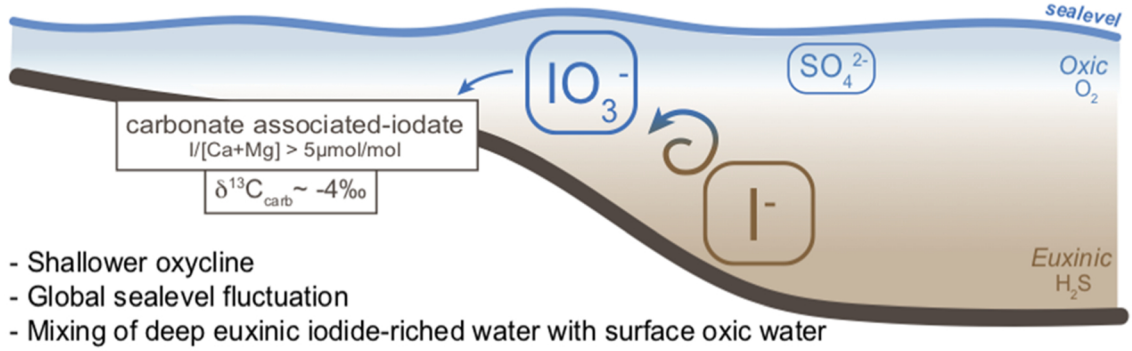

- Shallower oxycline
- Global sealevel fluctuation
- Mixing of deep euxinic iodide-riched water with surface oxic water
- Shuffling of iodide to iodate reservoir
- Iodate incorporation in shallow carbonates
- Nitrogen as a biolimiting nutrient

Figure 9